MNRAS **000**, 1–16 (2018) Preprint 26 October 2018 Compiled using MNRAS LATEX style file v3.0

Jets blowing bubbles in the young radio galaxy 4C 31.04

Henry R. M. Zovaro[1]★, Robert Sharp[1], Nicole P. H. Nesvadba[2], Geoffrey V. Bicknell[1], Dipanjan Mukherjee[3], Alexander Y. Wagner[4], Brent Groves[1], Shreyam Krishna[1]

[1]*Research School of Astronomy and Astrophysics, The Australian National University, Canberra, ACT 2611, Australia*
[2]*Institut d'Astrophysique Spatiale, UMR 8617, Université Paris-Sud, Bât. 121, 91405 Orsay, France*
[3]*Dipartimento di Fisica Generale, Universita degli Studi di Torino, Via Pietro Giuria 1, 10125 Torino, Italy*
[4]*University of Tsukuba, Center for Computational Sciences, Tennodai 1-1-1, Tsukuba, Ibaraki, Japan*

Accepted XXX. Received YYY; in original form ZZZ

ABSTRACT

4C 31.04 is a ∼ 100 pc double-lobed Compact Steep Spectrum source believed to be a very young Active Galactic Nucleus. It is hosted by a giant elliptical with a dense, inhomogeneous, multi-phase circumnuclear disc harbouring ∼ 10^9 $M_\odot$ of gas. To investigate jet-ISM interactions in this source, we use high spatial resolution, adaptive optics-assisted *H*- and *K*-band integral field Gemini/NIFS observations of 4C 31.04 to probe two new phases of the circumnuclear medium: (1) A warm (∼ 10^3 K) molecular gas phase, traced by ro-vibrational transitions of H_2, and (2), the warm ionised medium, traced by the [Fe II]$_{\lambda 1.644}$ line. The [Fe II] emission traces shocked, ionised gas launched out of the disc plane by a jet-blown bubble 300 – 400 pc in diameter, a factor ≈ 4 times larger than the radio jets, whilst the H_2 emission probes shock-excited molecular gas in the interior ∼ 1 kpc of the circumnuclear disc. Hydrodynamical modelling shows that the apparent discrepancy between the extent of the shocked gas and the radio emission can occur when the brightest regions of the radio plasma are temporarily halted by dense clumps in the disc, whilst small amounts of plasma can percolate through the porous ISM and form an energy-driven bubble that expands freely out of the disc plane. This bubble is filled with low surface-brightness synchrotron-emitting plasma, which may not be visible in existing VLBI observations of 4C 31.04 due to insufficient sensitivity. Additional radial flows of jet plasma percolate to ∼ kpc radii in the circumnuclear disc, driving shocks and accelerating clouds of gas, causing the H_2 emission.

Key words: galaxies: active – galaxies: evolution – galaxies: nuclei – ISM: jets and outflows

1 INTRODUCTION

Feedback processes involving active galactic nuclei (AGN) have long been known to be important drivers of galaxy evolution. Quasar winds and jets from powerful AGN are believed to be important in shaping the galaxy luminosity function and in establishing the observed correlations between the properties of the bulge and the supermassive black hole (Silk & Rees 1998; Tremaine et al. 2002; Croton et al. 2006; King & Pounds 2015, and references therein). On much smaller scales, AGN feedback processes are likely to be equally important: in particular, interaction between radio jets and the interstellar medium (ISM) on sub-kpc scales may have a significant impact upon the evolution of the host galaxy, particularly in the earliest stages of jet evolution.

Hydrodynamical simulations of jets propagating through an inhomogeneous ISM (Mukherjee et al. 2016; Wagner et al. 2016) have shown that star formation in the host galaxy can both be enhanced and inhibited by interactions between the jets and the ISM on sub-kpc scales. Sutherland & Bicknell (2007, henceforth SB07) demonstrated that the evolution of young radio galaxies can be separated into distinct stages: a 'flood-and-channel' phase, followed by the formation of an energy-driven bubble that creates a bow shock as it expands, after which the jet breaks free of the bubble, finally forming extended FR-II-like lobes. The expanding bubble driven by the jet plasma can ablate clouds and accelerate them to high velocities, preventing star formation and driving powerful outflows (e.g., in 3C 326 N; Nesvadba et al. 2010). Mukherjee et al. (2016) found that the energy-driven bubble can remain confined to the galaxy's potential for a long time due to interactions with the inhomogeneous ISM. The bubble drives shocks and turbulence into the ISM, potentially leading to quenching of star formation. Conversely, the over-pressured plasma in the hot bubble can trigger gravitational instabilities and cloud collapse, enhancing star formation (Gaibler et al. 2012; Fragile et al. 2017). Despite mounting evidence from simulations of such 'positive feedback', jet-induced star formation has only been observed in a handful of sources, e.g., the z = 3.8

★ E-mail: henry.zovaro@anu.edu.au

radio galaxy 4C 41.17 (Bicknell et al. 2000), 3C 285 (Salomé et al. 2015), Centaurus A (Salomé et al. 2017) and in Minkowski's Object (Salomé et al. 2015; Lacy et al. 2017). Simulations show these feedback mechanisms are sensitive to both the ISM structure and jet power, making it difficult to predict whether star formation will be enhanced or inhibited, and in turn the impact on the evolution of host galaxy (Wagner et al. 2016; Zubovas & Bourne 2017; Mukherjee et al. 2018a). High-resolution observations of the ISM in young radio galaxies are therefore key in exposing the relationship between the properties of the radio jets and the host galaxy.

Gigahertz Peak Spectrum (GPS) and Compact Steep Spectrum (CSS) sources are extragalactic radio sources characterised by a peak in their radio spectrum occurring in the GHz and MHz range for GPS and CSS sources respectively and a compact (< 1 kpc) radio emission with resolved lobes and/or jets (for a comprehensive review see O'Dea 1998). Recent observations (e.g., Tingay et al. 2015; Callingham et al. 2017) indicate that the spectral peak is most likely caused by free-free absorption (FFA) of synchrotron emission by an ionised ISM with a varying optical depth. Hydrodynamical simulations by Bicknell et al. (2018) have indeed demonstrated that jets percolating through an ionised, inhomogeneous ISM can reproduce the observed spectra of GPS/CSS sources by invoking FFA alone. The peaked spectrum and compact size of GPS and CSS sources suggests that they harbour young jets, temporarily confined by a dense ISM, and are the progenitors of classical double-lobed radio sources. This 'youth hypothesis' is supported by age estimates based on the decay of the synchrotron emission spectrum and on hotspot advance velocities (O'Dea 1998). The compact nature of the jets in GPS and CSS sources therefore enables us to study jet-ISM interaction within the host galaxy in the earliest stages of evolution, and therefore represent an important class of sources in the context of AGN feedback.

4C 31.04 is a low-redshift ($z = 0.0602$) CSS source with highly compact (~ 100 pc across) jets believed to be $\sim 10^3$ yr old (Giroletti et al. 2003, henceforth referred to as Gi03). The mottled and asymmetric radio morphology suggests strong interactions between the jets and a dense ISM. The proximity of 4C 31.04 enables us to probe jet-ISM interaction at the necessary sub-kpc scales with adaptive optics (AO)-assisted observations on an 8-metre telescope; nonetheless, no previous optical or near-infrared (IR) observations have resolved the host galaxy down to scales comparable to the size of the radio lobes.

With the aim of observing jet-induced AGN feedback in action, we observed 4C 31.04 with the Near-infrared Integral Field Spectrograph (NIFS) and the ALTAIR adaptive optics (AO) system on the Gemini North telescope in September 2016. In our NIFS observations, we probe both the warm molecular and ionised gas phases, both of which are important tracers of jet-ISM interaction. Many groups have carried out similar studies of young radio galaxies in the past (e.g., 3C 326 N Nesvadba et al. (2010, 2011), 4C 12.50 (Morganti et al. 2013), IC 5063 (Tadhunter et al. 2014; Morganti et al. 2015), NGC 1052 (Morganti et al. 2005), NGC 1068 (Riffel et al. 2014), NGC 1275 (Scharwächter et al. 2013), NGC 4151 (Storchi-Bergmann et al. 2012) and PKS B1718-649 (Maccagni et al. 2016)). However, the 100 pc-scale jets of 4C 31.04 provides a rare opportunity to observe jet-ISM interactions in the very earliest stages of evolution. Moreover, 4C 31.04 has a wealth of auxiliary data at multiple wavelengths, including milliarcsecond-resolution very long baseline interferometry (VLBI) imaging, that enable us to better constrain the properties of the jets and of the host galaxy.

In Section 2 we discuss the properties of 4C 31.04 and its host galaxy gleaned from previous multi-wavelength studies. Section 3 details our NIFS observations and data reduction method. In Section 4 we discuss the two distinct phases of the ISM we detect in our observations. We discuss the interpretation of our observations in the context of AGN feedback in Section 5 and summarise our findings in Section 6.

For the remainder of this paper, we assume a cosmology with $H_0 = 69.6$ km s^{-1} Mpc^{-1}, $\Omega_M = 0.286$ and $\Omega_{vac} = 0.714$, which corresponds to a luminosity distance $D_L = 271.3$ Mpc and spatial scale of 1.17 kpc arcsec^{-1} at the assumed redshift $z = 0.0602$ of 4C 31.04 (Wright 2006).

2 PREVIOUS OBSERVATIONS OF 4C 31.04

2.1 Host galaxy properties

The host galaxy of 4C 31.04 is MCG 5-4-18, a giant elliptical approximately 2 H-band magnitudes brighter than L_* at a redshift $z = 0.602$ (García-Burillo et al. 2007, henceforth Ga07). Willett et al. (2010) provide an upper limit of $M_{\rm BH} \leq 10^{8.16}$ M$_\odot$ on the mass of the central black hole using the [O IV]$_{25.4\ \mu m}$ width.

This host galaxy has a Seyfert 2-like optical spectrum consistent with a predominantly old, metal-rich stellar population (Serote Roos & Gonçalves 2004; Gonçalves & Serote Roos 2004). Despite this, there is evidence for moderate levels of star formation (SF): Willett et al. (2010) detect polycyclic aromatic hydrocarbon (PAH) emission and silicate absorption features in spatially unresolved *Spitzer* mid-IR spectroscopy, indicating gas and dust heating by both ongoing SF and AGN. Using *IRAS* 60 μm and 100 μm fluxes Ocaña Flaquer et al. (2010) find SFR$_{\rm FIR} \approx 4.9\ M_\odot$ yr^{-1}, comparable to that calculated by Willett et al. (2010) using PAH emission features (SFR$_{\rm PAH} = 6.4\ M_\odot$ yr^{-1}).

Perlman et al. (2001, henceforth Pe01) observed 4C 31.04 with the *Hubble Space Telescope* (*HST*) using the Wide Field Planetary Cam 2 (WFPC2) and NICMOS, revealing several obscuring dust features, including an edge-on circumnuclear disc with a pronounced warp. Mid-IR silicate absorption features indicate that the dust has a clumpy distribution (Willett et al. 2010). Previous multi-wavelength studies indicate that for a low-z radio host galaxy, 4C 31.04 harbours an unusually massive ($10^{10}\ M_\odot$) multi-phase circumnuclear disc. This is discussed further in Section 2.3.

4C 31.04 is the dominant member in a small group, with a spiral companion at a projected distance of ~20 kpc. Despite this, neither the galaxy nor its nearest neighbour show any sign of interaction on larger scales such as tidal tails; (Pe01) conclude any interaction must have taken place $\gtrsim 10^8$ yr ago.

2.2 Radio properties

4C 31.04 is a Compact Steep Spectrum (CSS) source, with $P_{1.4\ \rm GHz} = 10^{26.3}$ W Hz^{-1} (van Breugel et al. 1984) and a spectral peak at ~ 400 MHz (estimated from the spectrum available at the NASA/IPAC Extragalactic Database (NED)[1]). The source

[0] Based on observations made with the NASA/ESA Hubble Space Telescope, and obtained from the Hubble Legacy Archive, which is a collaboration between the Space Telescope Science Institute (STScI/NASA), the Space Telescope European Coordinating Facility (ST-ECF/ESA) and the Canadian Astronomy Data Centre (CADC/NRC/CSA).

[1] The NASA/IPAC Extragalactic Database (NED) is operated by the Jet Propulsion Laboratory, California Institute of Technology, under contract with the National Aeronautics and Space Administration.

has two edge-brightened radio lobes separated by ∼ 100 pc with a weak inverted-spectrum core (Cotton et al. 1995; Giroletti et al. 2003; Struve & Conway 2012). The axis of the jets is approximately East-West, with a PA ≈ 100°. The lobes are highly asymmetric, suggesting strong jet-ISM interaction (Giovannini et al. 2001). The Western lobe is relatively faint and diffuse, suggesting the jet is interacting with many small clouds (Bicknell 2002), whilst the Eastern lobe is brighter and more compact, and has a peculiar 'hole' that may be caused by an overdensity in the ISM that is impenetrable to radio plasma (Gi03).

Radio observations indicate 4C 31.04 is a truly young radio source. Low flux variability ($\lesssim$ 2% at 5 GHz) and polarisation ($\lesssim$ 1% at 5 GHz) in the lobes suggest beamed emission is unlikely (Gi03), and that the compactness of the source is unlikely an orientation effect. Giovannini et al. (2001) estimated that the jets are nearly coplanar with the sky, with an orientation angle $\theta \gtrsim 75°$. Differential VLBI imaging of 4C 31.04 has revealed the radio emission to be rapidly expanding, with hotspot velocities of ∼ 0.3c, yielding a dynamic age of ∼ 550 yr; synchrotron decay modelling yields much older radiative ages of 3300 yr and 4500 − 4900 yr in the Eastern and Western lobes respectively (Gi03).

2.3 Previous observations of the circumnuclear medium

A number of multi-wavelength studies have shown that 4C 31.04 has a multiphase and dynamically unrelaxed circumnuclear disc that contains dust, molecular gas and atomic gas.

The $R - H$ colour map of Pe01 (their Fig. 1a) reveals several obscuring structures surrounding the nucleus, including a reddened circumnuclear disc, loops streaming from the Northernmost point of the disc, and a large S-shaped structure extending to the North and South. The circumnuclear disc is approximately perpendicular to the radio jets, and extends roughly 500 pc to the North and 1000 pc to the South. The disc is highly inclined, viewed almost edge-on.

Using the IRAM 30 m telescope, Ocaña Flaquer et al. (2010) found double-horned ^{12}CO(2–1) and ^{12}CO(1–0) profiles with superimposed absorption, suggesting a massive inclined disc of molecular gas. Ga07 also detected a disc-like structure in the 1 mm continuum with the IRAM Plateau de Bure interferometer (PdBI) ∼ 1.4 kpc in size consistent with the dusty disc in the *HST* $R-H$ image. They also found HCO$^+$ (1 − 0) emission to the North and South of the nucleus, with kinematics consistent with a disc (their Fig. 1b). Struve & Conway (2012) detected H I absorption using VLBI observations, and estimated a column density $N_{\rm H} = 1.2{-}2.4{\times}10^{21}$ cm^{-2}. The velocity structure of the absorption is consistent with a large rotating disc of atomic gas coinciding with the kpc scale molecular disc. The H I optical depth is much higher in the Eastern lobe, indicating that the disc is inclined such that the Eastern lobe is viewed through a dense column of gas. This is consistent with earlier H I VLBI observations by Conway (1996), which also revealed a sharp 'edge' in the H I opacity in the Western lobe (their Fig. 1). Conway (1996) also detected high-velocity H I clouds and free-free absorption features in front of both lobes, which they attributed to the jets evaporating material off the inner edge of the circumnuclear disc.

Irregularities in the kinematics and morphology of gas and dust in the circumnuclear regions of the galaxy suggest unrelaxed dynamics. Pe01 fitted isophotes to the *HST* NICMOST F160W (H-band) image and found significant anisotropies in the ellipticity and a position angle (PA) that twists by tens of degrees in the innermost 2–4 kpc. Ga07 detected blueshifted (∼ 150 km s^{-1}) HCO$^+$ (1 − 0) absorption over the centre of the galaxy, whilst Struve & Conway (2012) detected a narrow, redshifted H I absorption component consistent with a cloud at a radius ≫ 100 pc falling into the nucleus, which may be a remnant of a merger or accretion event.

These observations show that the host of 4C 31.04 contains a dense, massive, circumnuclear disc, consisting of cold dust, both cold and warm molecular gas, and atomic gas. Twisted central isophotes and non-circular motions indicate that the disc is dynamically unrelaxed, perhaps due to a previous a merger or interaction, accretion of new material, or by a jet-ISM interaction.

3 OBSERVATIONS AND DATA REDUCTION

3.1 Observations

We observed 4C 31.04 using the Near-infrared Integral Field Spectrometer (NIFS) (McGregor et al. 2003) on the 8.1 m Gemini North telescope on Mauna Kea in Hawai'i. NIFS provides R ∼ 3500 J-, H- and K-band spectroscopy over a 3" × 3" field of view with 0.1" × 0.04" spaxels. NIFS is fed by the ALTAIR adaptive optics (AO) system which can be used in laser guide star (LGS) or natural guide star (NGS) mode to provide near-diffraction limited resolution.

We obtained H- and K-band observations of 4C 31.04 using NIFS and the ALTAIR AO system used in laser guide star (LGS) mode with a position angle of 0° on September 22, 2016 during program GN-2016B-C-1. We used 600 s exposure times for both source and sky frames, integrating on-source for a total of 80 and 60 minutes in H- and K-band respectively. The HIPPARCOS stars HIP12218, HIP117774 and HIP12719, observed before and after 4C 31.04, were used as telluric and flux standards.

3.2 NIFS data reduction in IRAF

We reduced the data using the Gemini IRAF package, reducing science frames for both object and standard star exposures as follows.

We subtract individual sky frames from the science frames, pairing the sky frames taken closest in time to the science frame. We divide through by a master flat field, then extract the slices from the science frames to form 3D data cubes. All data cubes are spatially interpolated to yield 0.05" × 0.05" square pixels. We then interpolate over bad pixels, apply the wavelength calibration and correct for spatial distortion. The wavelength solution was found using argon and xenon arc lamp exposures taken during the night, and spatial distortions were calibrated using an exposure of a Ronchi grating through a flat field.

To correct for telluric absorption lines, we generate a 1D spectrum of the telluric standard as follows. We co-add the spectra within an 0.5"-diameter aperture centred on the star, and flatten the resulting 1D spectrum by dividing it by a normalised blackbody corresponding to the temperature of the star, estimated from its spectral class. We fit and remove stellar absorption lines using a Voigt profile. We remove telluric absorption lines by dividing the object data cubes by the resulting 1D spectrum.

To flux calibrate the object data cubes, we use exposures of a standard star with a known magnitude to convert counts in the data cube into units of monochromatic flux density arcsec^{-2}. We generate a 1D spectrum of the flux standard in the same fashion as for the telluric standard, and multiply it by the normalised blackbody to restore its original spectral shape. We remove telluric absorption lines by dividing the spectrum by the 1D spectrum of the telluric standard. We then divide it by a blackbody spectrum in units of erg s^{-1} cm^{-2} Å^{-1} corresponding to the temperature of the flux calibration standard star. We fit a polynomial to the resulting spectrum to

give the transfer function. To flux calibrate the object data cubes, we divide the individual object data cubes by the transfer function, the exposure time and the spaxel area to give units of erg s^{-1} cm^{-2} $Å^{-1}$ $arcsec^{-2}$. Finally, we shift and median-combine each object data cube to yield a single data cube.

3.3 MAD smoothing

We use a Median Absolute Deviation (MAD) smoothing algorithm with a radius of 2 pixels to smooth the reduced data cubes and to remove artefacts. In each wavelength slice, for each pixel, we compute the median and standard deviation σ of the surrounding pixels out to the specified radius, and reject those pixels with absolute value greater than $n\sigma$ from the median. We iterate until no more pixels are rejected. The value of the central pixel is then replaced by the mean of the remaining pixels, and the variance of the central pixel is replaced by the mean of the variance of the remaining pixels.

Before smoothing, the angular resolution of our observations corresponds to a Full Width at Half Maximum (FWHM) of approximately 110 pc and 150 pc in the H- and K-bands respectively. After smoothing with a radius of 2 pixels, the resolution is decreased to approximately 160 pc and 190 pc in the H- and K-bands respectively.

3.4 Emission line fitting

We use `mpfit` (Markwardt 2009), a `python` implementation of the Levenberg-Marquardt algorithm (Moré 1978) developed by M. Rivers[2] to fit single-component Gaussian profiles to emission lines. We keep fits with $\chi^2 < 2$ and signal-to-noise ratio (SNR) > 1. In all reported linewidths, we have accounted for instrumental resolution by subtracting the width of the line spread function (LSF) in quadrature from the width of the fitted Gaussian. We estimate the width of the LSF by fitting a Gaussian to sky lines close in wavelength to the relevant emission line.

Integrated line fluxes and upper limits for emission lines in 4C 31.04 are shown in Table 1. To calculate integrated line fluxes, we simply sum the fluxes found in each spaxel.

To calculate upper limits for line fluxes which are not detected using our χ^2 and SNR criteria, we use the following method. In each spaxel, we calculate the standard deviation σ in the continuum in a window centred on the emission line. We assume the non-detected emission line in that spaxel is a Gaussian with amplitude 3σ. The width we use depends on the emission line. For non-detected ro-vibrational H_2 lines, we use the measured width of the H_2 1–0 S(1) emission line in that spaxel. For hydrogen recombination lines, we use the Gaussian sigma of 24.9 Å we calculate from the measured equivalent width of 18 Å for the combined Hα and [N II] lines in a single-slit optical spectrum of 4C 31.04 reported by Marcha et al. (1996). When quoting integrated upper limits, we assume the lines are detected in every spaxel in which we detect the H_2 1–0 S(1) emission line.

4 RESULTS

Diffraction-limited *HST* WFPC2 imaging has similar angular resolution to our NIFS observations (0.05”), enabling us to directly compare the two sets of observations. Fig. 1a shows the K-band continuum (red) from our NIFS observations overlaid onto the *HST* B-band image. Fig. 1b overlays the fluxes of the ro-vibrational H_2 emission (blue) we detect in the K-band and the [Fe II]$_{\lambda 1.644}$ emission (green) we detect in the H-band onto the *HST* $R-H$ image, placing both in context. The H_2 emission traces the dusty disc, and shows hints of a warp to the North and South, suggesting the H_2 is part of the large S-shaped dust feature. Meanwhile, the [Fe II] emission is localised to the nucleus.

4.1 Nuclear [Fe II] emission

In our H-band observations we detect [Fe II] $a^4D_{7/2} - a^4F_{9/2}$ (rest-frame wavelength 1.644 μm) emission in the inner few 100 pc of 4C 31.04. Fig. 2 shows the H-band continuum and the [Fe II] line flux, radial velocity and velocity dispersion.

We measure the spatial extent of the [Fe II] emission by fitting a 2D Gaussian to the integrated flux map. The emitting region is marginally resolved in our observations and is elongated, extending over $\approx$ 380 pc E-W and $\approx$ 320 pc N-S. The line profile is flat, asymmetric and broad, with a velocity dispersion of approximately 350 km s^{-1} across the emitting region. We argue that the [Fe II] emission traces gas being accelerated out of the plane of the circumnuclear disc by the jet-driven bubble, which we discuss further in Section 5.

4.2 H_2 emission

We detect the H_2 1–0 S(1), S(2) and S(3) emission lines in our K-band spectra, corresponding to transitions involving changes in the rotational quantum number with $\Delta J = +2$ and the vibrational level transition $v = 1$ to $v = 0$. These *ro-vibrational* emission lines trace warm H_2 between $\sim 10^3 - 10^4$ K. In Fig. 3, we show the flux distribution, radial velocity and velocity dispersion of the H_2 1–0 S(1) line we detect in our NIFS observations. The flux extends over $\approx$ 2 kpc from North to South, and the radial velocity shows large-scale rotation, indicating that the warm H_2 is a part of the kpc-scale circumnuclear disc observed in CO, HCO^+ and H I. The flux peaks sharply at the nucleus (Fig. 3): indeed, we find that $\approx$ 20% of the total flux is contained within the central 0.4”. In this section, we analyse the inner 0.4” separately to the remaining H_2 emission in order to determine any differences in the excitation mechanism and temperature between the central and extended components.

4.2.1 *Kinematics*

To determine whether the H_2 belongs to the circumnuclear disc, we fit a simple disc model to our data using `mpfit`. Our model has solid-body rotation out to a break radius r_b, and a flat rotation curve for $r > r_b$, and we fit the systemic velocity as a free parameter. We do not account for beam smearing in the fit. Fig. 4 shows the model fit and residuals. The disc fit has a PA approximately perpendicular to the jet axis, indeed consistent with that of the existing circumnuclear disc. The fitted inclination of the disc is consistent with the Easternmost edge being closest to us, which is also consistent with the greater H I opacity of the Eastern radio lobe (Conway 1996; Struve & Conway 2012). At the edge of the disc ($r \approx 0.8$ kpc), the rotational velocity $v_c \approx 425$ km s^{-1} with respect to the systemic velocity, comparable to that of the HCO^+ emission (Ga07). Therefore, our disc fit shows the warm H_2 probes the interior $\sim$ kpc of the circumnuclear disc of 4C 31.04, where

[2] Available `http://cars9.uchicago.edu/software/python/mpfit.html`.

Table 1. Emission line fluxes and their uncertainties. The integrated flux is measured by adding together the emission line fluxes in each individually fitted spaxel. Upper limits are computed using the method described in Section 3. All quantities are given in units of erg s^{-1} cm^{-2}.

Line	Total Integrated flux (erg s cm^{-2})	$r \leq 0.4''$	$r > 0.4''$
H_2 1–0 S(1)	$3.04 \pm 0.07 \times 10^{-16}$	$6.0 \pm 0.3 \times 10^{-17}$	$2.45 \pm 0.04 \times 10^{-16}$
H_2 1–0 S(2)	$5.06 \pm 0.06 \times 10^{-17}$	$2.3 \pm 0.2 \times 10^{-17}$	$2.8 \pm 0.2 \times 10^{-17}$
H_2 1–0 S(3)	$2.87 \pm 0.13 \times 10^{-16}$	$7.1 \pm 0.4 \times 10^{-17}$	$2.16 \pm 0.05 \times 10^{-16}$
H_2 2–1 S(1)	$\leq 3.698 \times 10^{-16}$	$\leq 2.302 \times 10^{-17}$	$\leq 3.467 \times 10^{-16}$
H_2 2–1 S(2)	$\leq 2.599 \times 10^{-16}$	$\leq 1.911 \times 10^{-17}$	$\leq 2.408 \times 10^{-16}$
H_2 2–1 S(3)	$\leq 3.872 \times 10^{-16}$	$\leq 2.26 \times 10^{-17}$	$\leq 3.646 \times 10^{-16}$
H I Brγ	$\leq 5.491 \times 10^{-16}$	$\leq 3.908 \times 10^{-17}$	$\leq 5.1 \times 10^{-16}$
[Fe II]$_{\lambda 1.644}$	$6.4 \pm 0.2 \times 10^{-17}$	—	—

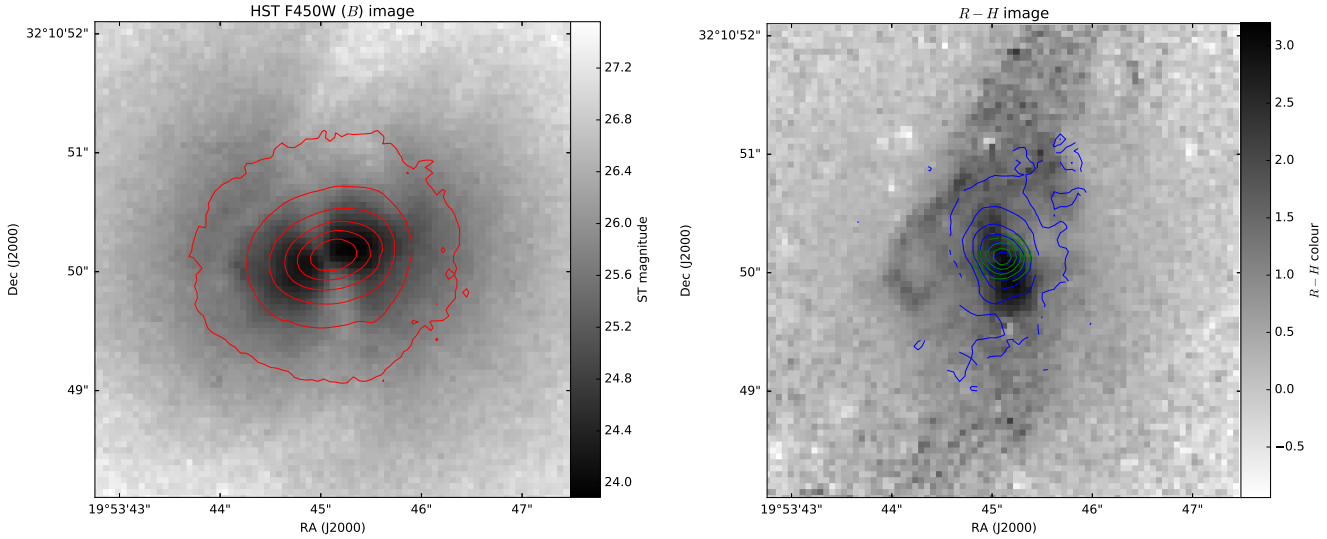

(a) (b)

Figure 1. Our K-band NIFS observations overlaid onto *Hubble Space Telescope* images[4]. (a) shows the NIFS K-band continuum (red contours) overlaid onto the *HST* WFPC2 B-band (F450W) image. The K-band contours represent the underlying stellar mass distribution, showing that the 'cones' to the East and West of the nucleus are not physical features, but a result of dust obscuration. The contours in (b) show the flux of the H_2 1–0 S(1) (blue) and [Fe II]$_{\lambda 1.644}$ (green) emission lines overlaid onto the *HST* $R-H$ image. Whilst the [Fe II] emission is concentrated to the central few 100 pc, the H_2 emission extends to $\sim$ 1 kpc North and South of the nucleus, suggesting it is part of the massive circumnuclear disc.

Table 2. Emission line ratios. The integrated flux is measured by adding together the emission line fluxes in each individually fitted spaxel. Upper limits are computed using the method described in Section 3..

Line ratio	Total	$r \leq 0.4''$	$r > 0.4''$
H_2 1–0 S(1)/H I Brγ	0.5540	1.5212	0.4799
H_2 1–0/2–1 S(1)	0.7856	2.6304	0.6712
[Fe II]$_{\lambda 1.644}$/Brγ	1.06294	1.06294	—

the solid-body rotation is a result of the warm H_2 not extending far enough into the disc to reach the turnover in the rotation curve.

Interestingly, the H_2 emission has a net blueshifted velocity of $\approx$ 150 km s^{-1} relative to the systemic velocity derived using the redshift, which is markedly similar to that of HCO^+ (Ga07) and H I (Struve & Conway 2012) viewed in absorption over the nucleus . A uniform distribution of dust in the disc could cause the flux-weighted mean velocity to have a significant blueshift; however this scenario would require an unrealistically large A_K. We instead speculate that the warm H_2 traces clouds of gas being radially accelerated by jet plasma percolating through the disc, and that the net blueshift is because redshifted gas on the far side of the disc is obscured by extinction. We discuss this further in Section 5.

The velocity residuals of the disc fit (Fig. 4) reveal redshifted and blueshifted velocity residuals to the NE and SW of the nucleus respectively which are similar to the radial velocity of the [Fe II] emission (Fig. 2), suggesting the kinematics of the molecular disc could be disrupted by the same processes causing the [Fe II] emission. However, referring to the *HST* $R-H$ image (Fig. 1) and to the flux distribution of the warm H_2 (Fig. 3), the circumnuclear disc is clearly warped. The residuals in Fig. 4 could simply arise from our disc fit not accounting for this warp, and so this alone cannot be interpreted as evidence of kinematically disturbed molecular gas in the inner regions of the disc.

4.2.2 *Gas temperature*

If H_2 is in thermal equilibrium, the Boltzmann equation describes the level populations of the vibrational states. To determine whether or not the molecular gas is in thermal equilibrium, we use an excitation diagram, where we plot the level populations estimated from emission line fluxes as a function of the level energy (see Fig. 6).

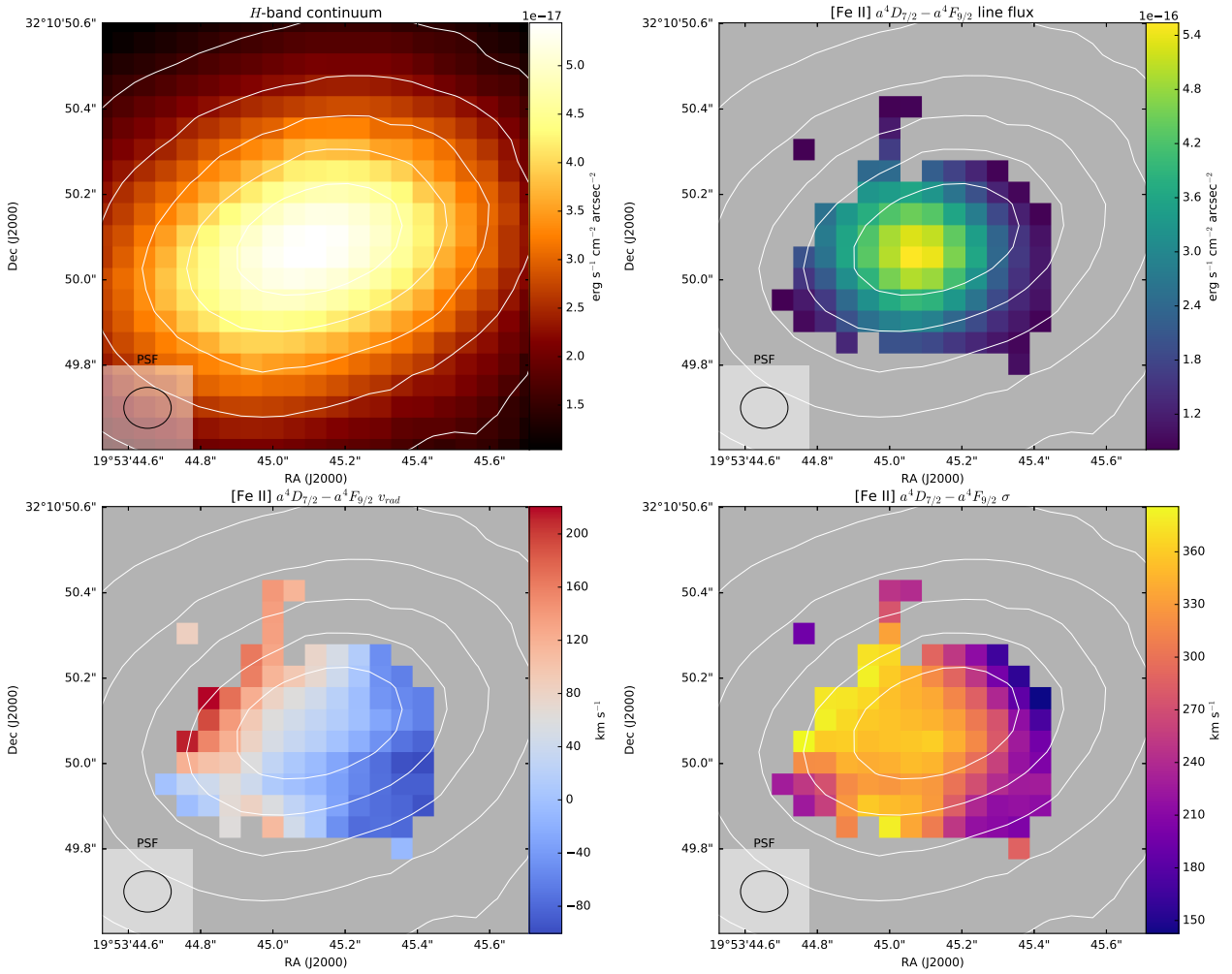

Figure 2. Clockwise, starting top left: the H-band continuum, integrated flux, radial velocity (minus the systemic velocity of the galaxy obtained from the redshift of $z = 0.0602$) and velocity dispersion (Gaussian σ) of the [Fe II]$_{\lambda 1.644}$ emission line. The H-band continuum is indicated in contours and the FWHM of the PSF (taking into account the effects of MAD smoothing) is indicated in all figures.

This also enables us to constrain the temperature of the warm H_2. If the gas is in thermal equilibrium, the points will lie along a straight line in log space of level population versus transition energy with slope $-1/T_{\rm kin}$ where $T_{\rm kin}$ is the kinetic temperature of the gas. To convert emission line fluxes to level populations we use the method described in Rosenberg et al. (2013):

$$\frac{N_{\rm obs}(v_u, J_u)}{g_u} = \frac{4\pi\lambda_{u,l}}{hc}\frac{I_{\rm obs}(u,l)}{A(u,l)}, \quad (1)$$

where $N_{\rm obs}(v_u, J_u)$ is the observed column density of H_2 molecules in the upper level u, g_u is the statistical weight of the upper level, $\lambda_{u,l}$ is the rest-frame wavelength corresponding to the transition, $I_{\rm obs}(u,l)$ is the measured flux of the transition and $A_{u,l}$ is the spontaneous emission coefficients, here obtained from Wolniewicz et al. (1998).

The excitation diagram for the H_2 1–0 S(1), S(2) and S(3) transitions in both the central and extended components of the H_2 is shown in Fig. 6, where we plot $N_{\rm obs}(v_u, J_u)/g_u$ as a function of the temperature corresponding to the transition energy of each line. For non-detected emission lines we use the upper limits in these regions (Table 1). Unfortunately due to the close spacing in temperature of the H_2 1–0 S(1,2,3) transitions, and because we only have upper limits for the H_2 2–1 S(1,2,3) lines, we cannot place a very restrictive constraint on the temperature in the extended component of the H_2; however, the emission line fluxes in the central 0.4" are consistent with a temperature 5000 – 6000K, indicating that the H_2 in the central regions is much hotter than the $\sim$ 300 K H_2 probed by *Spitzer* observations (Willett et al. 2010).

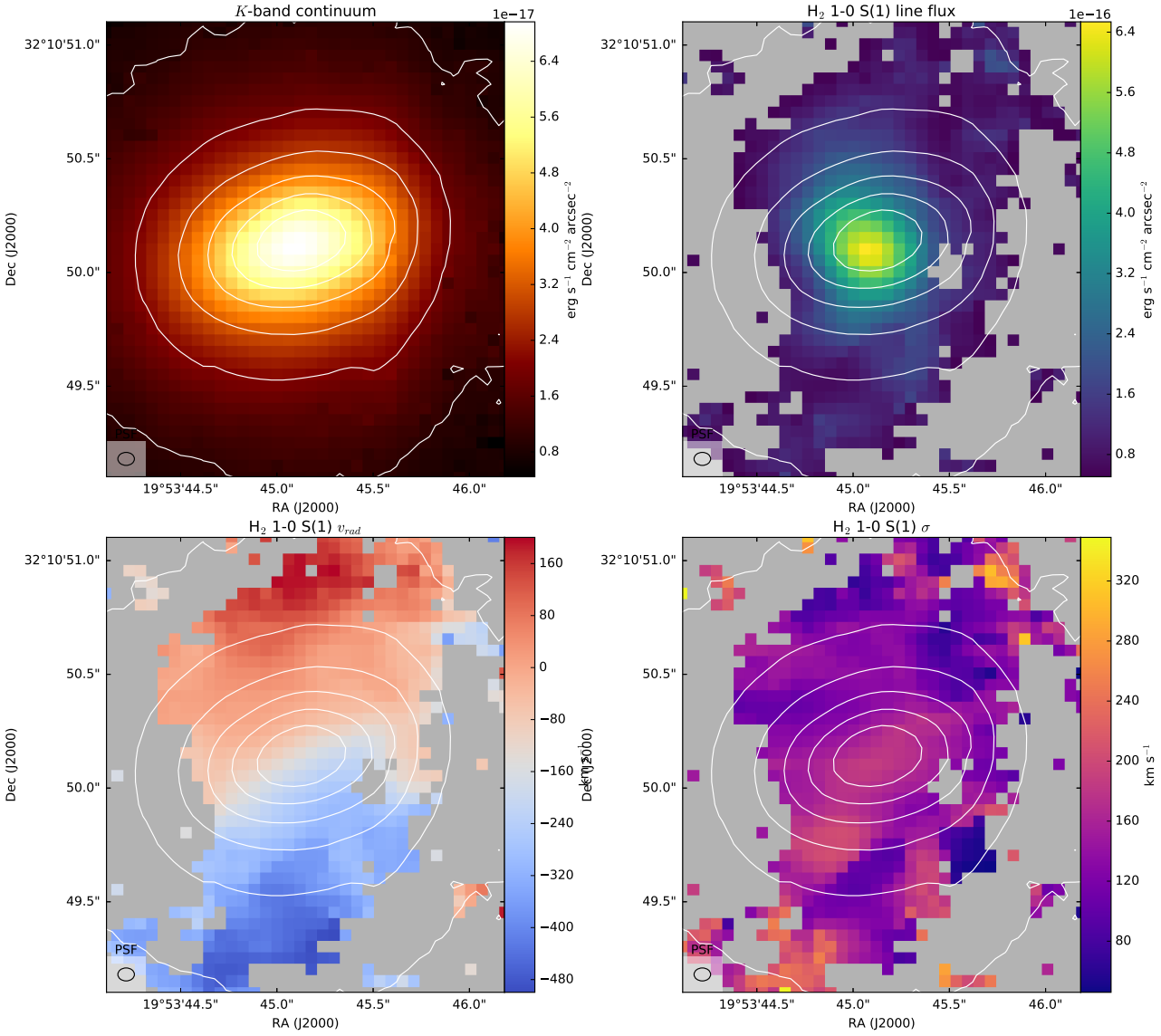

Figure 3. Clockwise, starting top left: the K-band continuum, integrated flux, radial velocity (minus the systemic velocity of the galaxy obtained from the redshift of $z = 0.0602$) and velocity dispersion (Gaussian σ) of the H_2 1–0 S(1) emission line. The K-band continuum is indicated in contours and the FWHM of the PSF (taking into account the effects of MAD smoothing) is indicated in all figures.

4.2.3 Excitation mechanism

Ro-vibrational H_2 emission can trace collisionally excited gas processed by shocks that are not fast enough to dissociate H_2 molecules. These emission lines can also be emitted by H_2 molecules excited by fluorescence from UV photons from O and B-type stars. We use two key emission line ratios (Table 2) to demonstrate that shock excitation is the most likely scenario.

Shock-excited H_2 can be distinguished from H_2 excited by a UV stellar radiation field by the relative level populations: fluorescent excitation tends to populate higher-level v states more than shock excitation. Therefore line ratios of ro-vibrational emission lines involving the same J state transition with different upper v levels are good indicators of the excitation mechanism. In shock-heated gas, the ratio of the H_2 1–0/2–1 S(1) lines tends to be much larger than in fluorescently-excited gas (e.g., Nesvadba et al. 2011). Fig. 7b shows this ratio in each spaxel. We have used upper limits to estimate the 2–1 S(1) flux; therefore these values should be interpreted as lower limits for the true line ratio. In the inner 0.4", the ratio of the integrated fluxes of the two lines exceeds ~ 2, indicating shock excitation.

At high enough densities ($n \gtrsim 10^3$ cm^{-3}), where H_2 is in LTE,

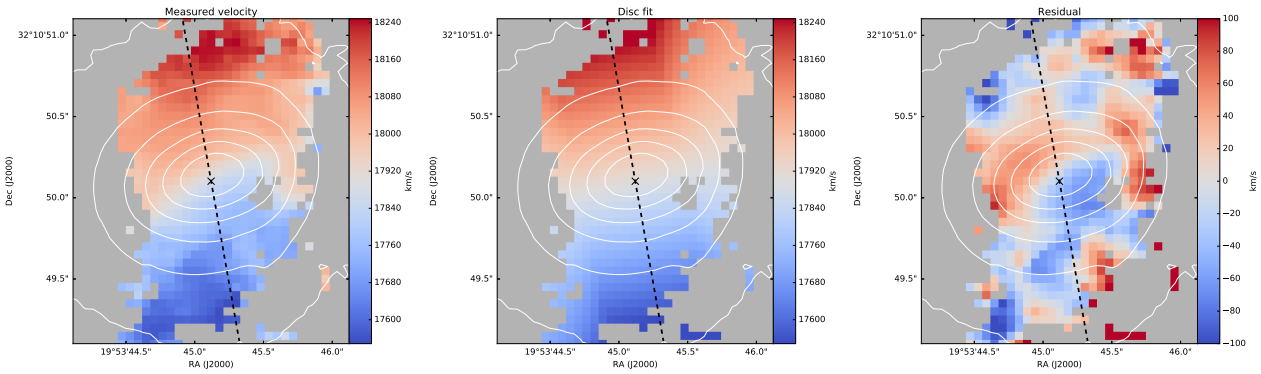

Figure 4. Kinematics the H_2 1–0 S(1) emission line. From left to right: measured radial velocity, radial velocity of the model fit, and the residual. With the exception of the residual plot, all velocities are given with respect to the local standard of rest. The cross represents the location of the nucleus (i.e., the peak in the K-band continuum). Fig. 5 shows a cross-section of the radial velocities taken along the dashed black line.

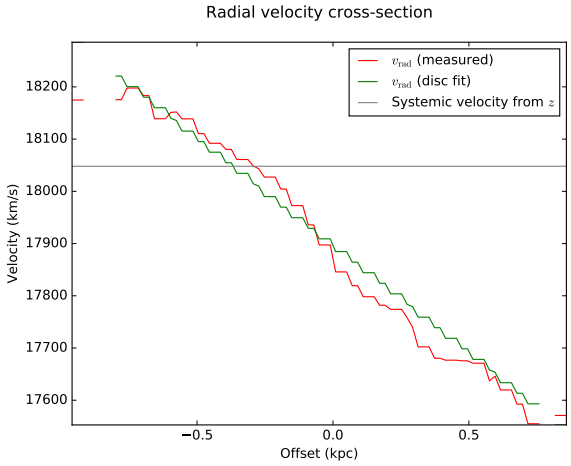

Figure 5. A cross section of the measured (red) and model fit (green) radial velocity taken along the black dashed lines indicated in Fig. 4. The systemic velocity of the galaxy, as estimated from the redshift, is indicated by the horizontal line, showing that the H_2 emission has a systemic blueshift of ≈ 150 km s^{-1}.

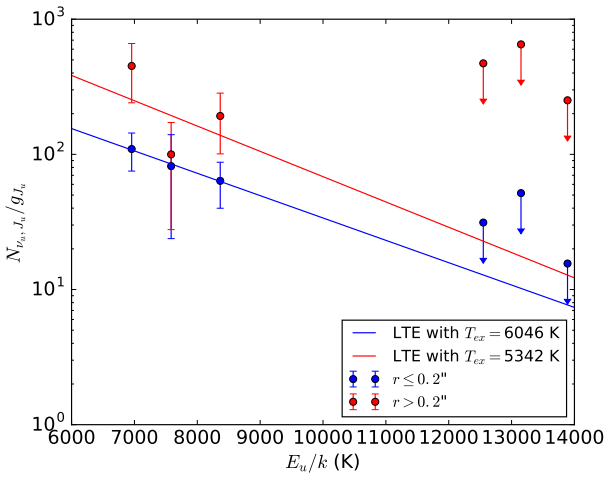

Figure 6. Excitation diagram of H_2. Round and square points indicate H_2 ro-vibrational 1–0 and 2–1 S(1), S(2) and S(3) transitions respectively. Red and blue points indicate estimates of $N_{\rm obs}(v_u, J_u)/g_u$ for the extended ($r > 0.2''$) and central ($r \leq 2''$ regions respectively. Circles indicate emission lines for which we can only estimate upper limits.

level populations will be similar in both shock- and fluorescent-excited H_2, in which case the line ratios are misleading. Here, we can eliminate fluorescent excitation by young stars because we do not detect Brγ, leaving shocks as the likely culprit. Fig. 7a shows the ratio H_2 1–0 S(1)/Brγ in each spaxel, where we have used upper limits to estimate the Brγ flux. In the inner 0.4", the ratio of the integrated fluxes of the two lines exceeds the 0.1–1.5 expected when the excitation source is UV heating in star-forming galaxies (Puxley et al. 1990). Additionally, our Brγ upper limits are pessimistic, because we assume a Gaussian sigma determined from the combined Hα+[N II] equivalent width of Marcha et al. (1996) from an unresolved spectrum. Therefore, combining this result with the high H_2 1–0/2–1 S(1) ratio, we conclude that the ro-vibrational H_2 emission is excited by shocks in the central region.

In the extended component, we cannot rule out star formation as the source of excitation, although we note these results are not inconsistent with shock excitation, because both line ratios involve upper limits.

4.2.4 *Mass estimates*

We now estimate the dynamical mass and warm gas mass and compare our results with those from previous studies in Section 2.3.

Solid-body rotation in the H_2 radial velocity implies the mass distribution interior to the disc can be approximated as a uniform-density sphere. We estimate the enclosed dynamical mass using $M_{\rm dyn} = v_c(r)^2 r/G$ where $v_c(r) \propto r$ is the rotational velocity at radius r and G is the gravitational constant. From our best-fit thin-disc model, the rotational speed of the disc at its edge is $v_c(r = 0.8\,\text{kpc}) \approx 425$ km s^{-1} and a dynamical mass $M_{\rm dyn} \approx 3.4 \times 10^{10}\ M_\odot$.

Dale et al. (2005) assumes LTE conditions and a temperature of 2000 K to derive an expression for the mass of warm H_2 using the H_2 1–0 S(1) flux $F_{1\text{–}0\ \text{S(1)}}$:

$$M(\text{H}_2)_{\rm warm} \approxeq 5.08\ M_\odot \left(\frac{F_{1\text{–}0\ \text{S(1)}}}{10^{-16}\ \text{W m}^{-2}}\right)\left(\frac{d}{\text{Mpc}}\right)^2 . \quad (2)$$

Using this method we obtain $M(\text{H}_2)_{\rm warm} = 1140\ M_\odot$. We note that

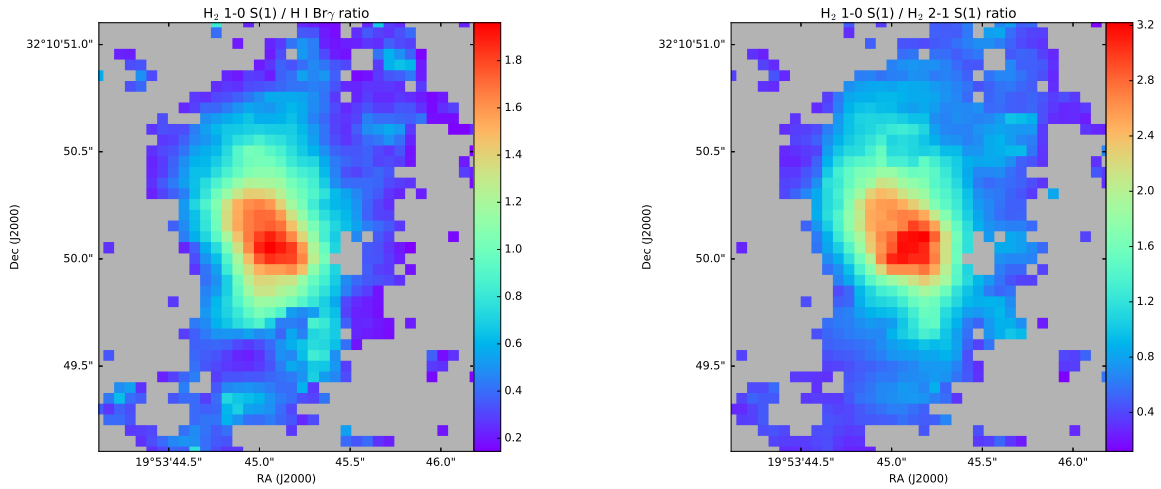

(a) (b)

Figure 7. Emission line ratio maps that we use to determine the excitation mechanism for the warm H_2 in different regions. (a) shows the H_2 1–0 S(1)/Brγ ratio and (b) shows the H_2 1–0 S(1)/H_2 2–1 S(1) ratio, and the black circle encloses the central 0.4". The values of ~ 2 and ~ 3 in the inner 0.4" in (a) and (b) respectively suggest shocks, and not star formation, are the likely excitation mechanism in the circumnuclear region.

Table 3. Mass estimates of different gas phases in 4C 31.04.

Phase	Mass ($M_\odot$)	Reference
$M_{\rm BH}$	$\leq 10^{8.16}$	Willett et al. (2010)
$M_{\rm dyn}$ ($r < 0.8$ kpc)	3.4×10^{10}	This work
$M_{\rm H_2, T=2000\ K}$	1140	This work
$M_{\rm H_2, T=338\pm100\ K}$	$(4.7 \pm 1.3) \times 10^6$	Willett et al. (2010)
$M_{\rm H_2, cold}$	$(60.63 \pm 16.92) \times 10^8$	Ocaña Flaquer et al. (2010)
$M_{\rm H\,I}$	4.8×10^7	Perlman et al. (2001)
$N_{\rm H\,I}$	$(1.2 - 2.4) \times 10^{21}$ cm^{-2}	Struve & Conway (2012)

we are only able to place an upper limit of $\approx 6 \times 10^4$ K on the H_2 temperature using our excitation diagram (Fig. 6), hence this mass is an approximate estimate.

Willett et al. (2010) also estimate $M(H_2)_{\rm warm}$ using mid-IR pure rotational (0–0) H_2 emission lines from *Spitzer* observations. For 4C 31.04 they find $M(H_2)_{\rm warm} = (4.7 \pm 1.3) \times 10^6\ M_\odot$ at a temperature $T = 338 \pm 100$ K, a factor $\sim 10^3$ higher than the mass we find. Combined with the temperature constraints provided by our excitation diagram (Fig. 6), we conclude that the ro-vibrational emission we detect in our NIFS observations traces a small fraction of the overall H_2 which is much hotter than the bulk of the gas probed by the pure rotational H_2 emission.

Table 3 compares the mass estimates of different ISM phases of 4C 31.04 from this work and the literature. We assume that the most reliable estimate of the cold H_2 gas mass is that of Ocaña Flaquer et al. (2010) derived from CO measurements, which gives a warm H_2 mass fraction of $\sim 10^{-6}$.

5 DISCUSSION

In this section, we analyse the energetics, kinematics and morphology of the [Fe II] and H_2 emission and argue that they indicate strong jet-ISM interaction is occurring in 4C 31.04.

Hydrodynamical simulations have shown that young, compact jets such as those in 4C 31.04 are capable of influencing the evolution of their host galaxies by injecting turbulence and driving shocks into the ISM (e.g., Sutherland & Bicknell 2007; Wagner & Bicknell 2011; Mukherjee et al. 2016, 2018b,a). Importantly, the coupling efficiency of the kinetic energy and momentum from the jet into the ISM peaks in these early stages of jet evolution (Wagner & Bicknell 2011; Mukherjee et al. 2016), making it an important epoch in the context of jet-driven feedback.

In the 'energy-driven bubble' stage, the jets become deflected and split as they encounter dense clumps in the ISM, forming streams of plasma that percolate through the ISM over a broad solid angle. Midplane density and temperature slices of a hydrodynamical simulation showing this phenomenon are shown in Fig. 8, with corresponding synthetic radio images shown in Fig. 9. The jet plasma inflates a high pressure, pseudo-spherical, energy-driven bubble that drives a forward shock into the ISM, dispersing clouds and accelerating them outwards. The low-density synchrotron-emitting plasma in the bubble cavity manifests as extended, low surface brightness radio emission (e.g., Fig. 5 in Wagner & Bicknell 2011). Simulations of jets propagating into dense, clumpy discs (Mukherjee et al. 2018a) have shown that jets may also drive subrelativistic flows of plasma into the disc plane, inducing shocks and turbulence. The jet plasma ablates clouds, and triggers hydrodynamical instabilities that form filaments. Ram pressure and thermal pressure gradients from shocks accelerates these clouds and filaments in a radial direction, introducing significant non-circular motions into the disc.

Our observations, together with its young age and small size, show that the radio jets of 4C 31.04 are in the 'energy-driven bubble' stage, where the jets are interacting strongly with the dense and clumpy circumnuclear disc. By comparing our observations with hydrodynamical simulations, we formulate the model shown in Fig. 10,

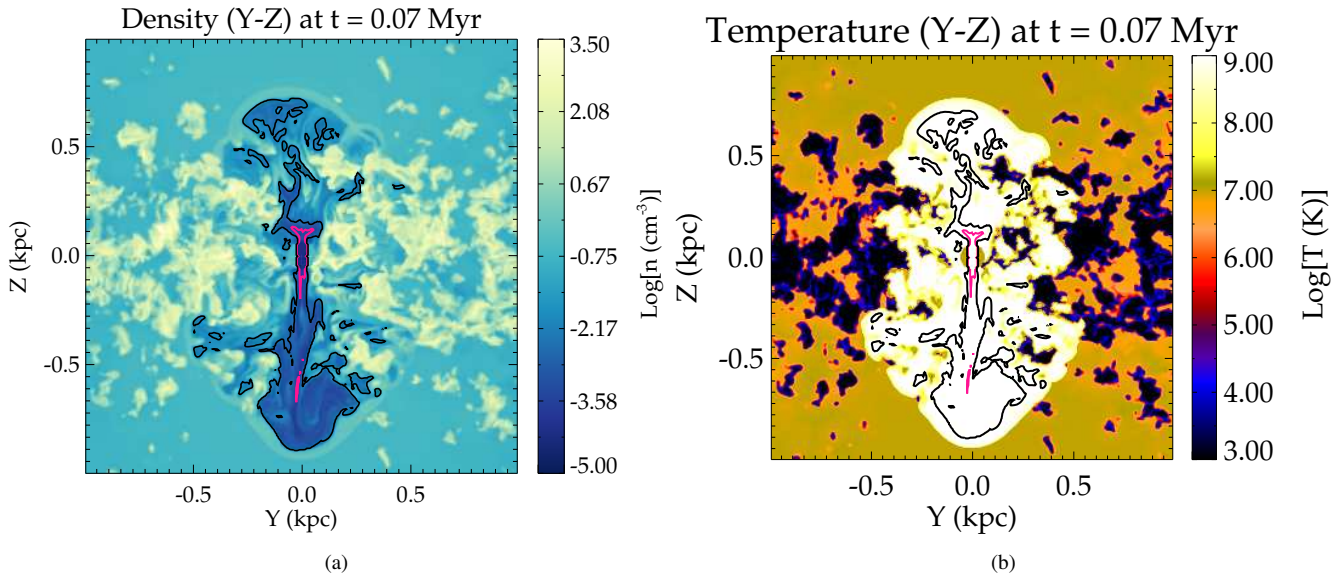

Figure 8. Mid-plane slices from a hydrodynamical simulation of a jet with $F_E = 10^{45}$ erg s^{-1} propagating in the Z-direction through a clumpy disc at an angle of 20° (model C of Mukherjee et al. (2018a); see their Table 2 for simulation parameters); (a) shows the density and (b) shows the temperature. The magenta contours represent jet plasma that will emit brightly in the radio (jet tracer $\phi = 0.5$) and the black contours trace much fainter plasma ($\phi = 0.005$) which fills the jet-driven bubble and drives shocks into the surrounding ISM.

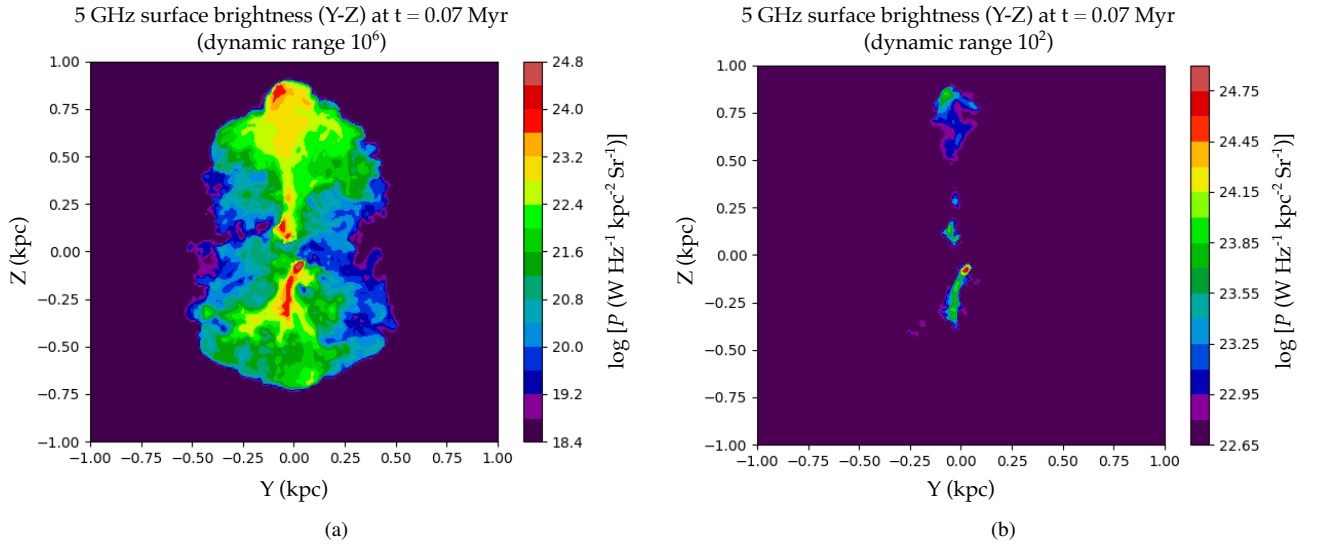

Figure 9. Synthetic radio surface brightness maps corresponding to the simulated mid-plane density and temperature slices shown in Fig. 8 at rest-frame 5 GHz with dynamic ranges of 10^2 and 10^6 respectively. The axis labels labels are in kpc and the intensity is given in $\log\left[P(\mathrm{W\ Hz^{-1}\ kpc^{-2}\ Sr^{-1}})\right]$. Comparing (a) and (b) demonstrates that a high dynamic range may be necessary to observe low surface brightness plasma extending beyond the radio lobes into the jet-driven bubble. We note that the dynamic range of Figure (b) is comparable to that of the 5 GHz VLBI observations of 4C 31.04 by Gi03, suggesting that higher dynamic range observations could reveal jet plasma out to the extent of the [Fe II] emission we observe in 4C 31.04.

which shows a top-down cross-sectional view of the circumnuclear disc of dust and atomic and molecular gas orbiting the nucleus. The inclination of the disc is such that the Eastern radio lobe is obscured, which is consistent with the greater H I opacity on that side (Conway 1996; Struve & Conway 2012). The 100 pc-scale radio lobes (dark green) shown to scale. The jet plasma inflates an expanding bubble which drives fast shocks into the surrounding ISM, destroying dust grains and launching material out of the disc plane, which is traced by [Fe II] (red) and high-velocity H I clouds (white circles) detected in absorption by Conway (1996). Shocked ionised gas (grey circles) free-free absorbs synchrotron emission from the jet plasma, causing the spectral turnover at 400 MHz. The jet plasma also drives radial flows into the disc, decelerating as it shocks molecular gas (blue), causing ro-vibrational H_2 emission. The plasma may also radially accelerate this gas to speeds $\sim$ 100 km s^{-1}, giving rise to non-circular motions including blueshifted H_2 emission and HCO^+ and H I absorption.

5.1 Updated jet flux estimate

Comparing the jet flux with observed emission line luminosities is important in determining whether it is plausible for the jets to be

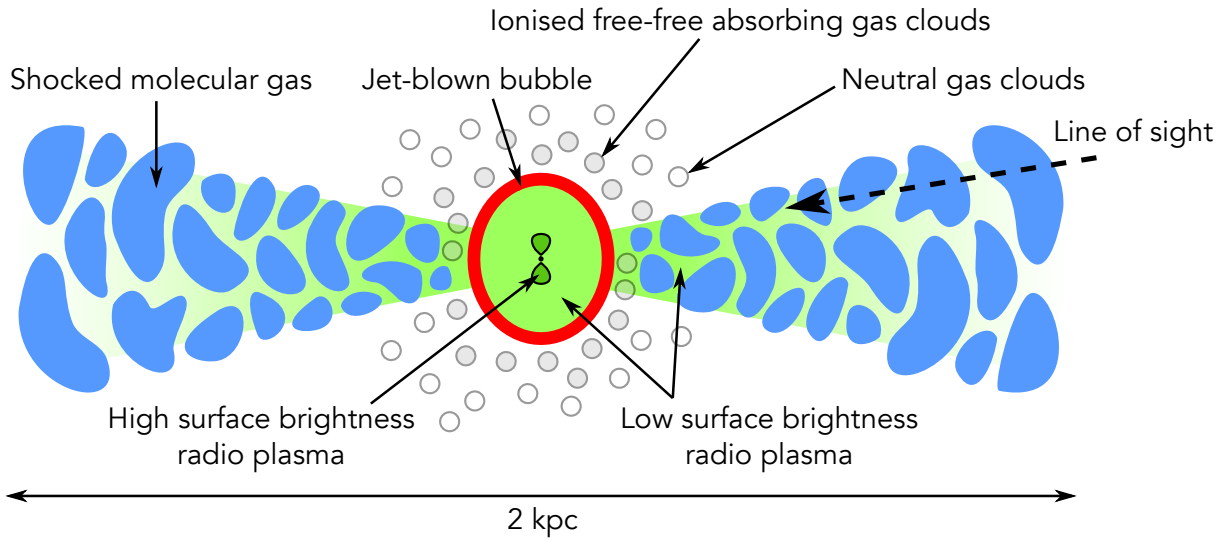

Figure 10. A top-down cross-section view of 4C 31.04 showing different components of the shocked gas in context, approximately to scale. Indicated in dark green are the 100 pc-scale radio lobes visible in VLBI observations Giovannini et al. (2001); Giroletti et al. (2003). The pale green region represents low surface-brightness jet plasma filling the jet-driven bubble, which drives a shock into the surrounding gas and causes [Fe II] emission (red). Jet plasma also percolates radially through channels in the clumpy circumnuclear disc (blue), driving shocks into neutral gas and causing H_2 emission. Clouds of ionised gas that free-free absorb synchrotron radiation from the jet plasma cause the spectral turnover at 400 MHz are indicated in grey circles. The white circles represent clouds of neutral gas. The line of sight is indicated by the dashed line; the disc is inclined such that the Western lobe is partially obscured by the disc, whereas the Eastern lobe is completely obscured by the disc, in line with the H I absorption map (Conway 1996; Struve & Conway 2012).

causing the line emission. Hence, before we discuss the excitation mechanisms for the [Fe II] and H_2 emission, we provide an updated estimate of the jet flux of 4C 31.04.

SB07 estimate the jet flux in 4C 31.04 by calculating the minimum energy density in the radio lobes to produce the observed synchrotron flux in 1.7 GHz VLBI observations, and find 4.4×10^{43} erg s^{-1} and 1.5×10^{43} erg s^{-1} in the Western and Eastern lobes respectively. We follow the same minimum energy method to calculate the jet flux, this time using higher resolution VLBI observations of Gi03 to achieve an improved estimate. Our input and output parameters are shown in Table 4. Using their 5 GHz VLBA image, we divide both East and West lobes up into sections of approximately constant flux density. We model each section as volume with depth L along the line of sight, which we assume to be equal to its width. We assume the volumes contain a randomly oriented magnetic field of strength B and a relativistic electron population with distribution $N(\gamma) = K\gamma^{-a}$ for $\gamma \in [\gamma_1, \gamma_2]$. In this simple model, the minimum energy density required to produce a given specific intensity of synchrotron emission I_ν is

$$\varepsilon_{\mathrm{min,tot}} = (1 + c_E)\epsilon_{e,\mathrm{min}} + \frac{B^2_{\mathrm{min}}}{2\mu_0} \tag{3}$$

where $\epsilon_{e,\mathrm{min}}$ is the minimum energy density in relativistic electrons and c_E represents the energy fraction in other species, which we assume to be 0. The minimum energy magnetic field and energy density in particles are given by

$$B_{\mathrm{min}} = \frac{m_e}{e}\left[\frac{a+1}{2}(1+c_E)C_2(a)^{-1}\frac{c}{m_e}\left(\frac{I_\nu \nu^\alpha}{L} f(a,\gamma_1,\gamma_2)\right)\right]^{\frac{2}{a+5}}$$
$$\varepsilon_{p,\mathrm{min}} = \frac{4}{a+1}\frac{B^2_{\mathrm{min}}}{2\mu_0} \tag{4}$$

respectively, where $\alpha = (a-1)/2$ is the spectral index of the synchrotron emission and $C_2(a)$ and $f(a, \gamma_1, \gamma_2)$ are constants. We find $\varepsilon_{p,\mathrm{min}} \sim 10^{-5}$ erg cm^{-3} and $B_{\mathrm{min}} \sim 10^{-2}$ G in all parts of the radio lobes.

Table 4. Parameters used in determining the jet flux. Output parameters are denoted with daggers (†).

Parameter	Symbol	Value
Min. electron Lorentz factor	γ_1	10^2
Max. electron Lorentz factor	γ_2	10^5
Age of radio lobes (Gi03)	t_{lobe}	5000 yr
Temperature of ambient ISM	T_a	10^7 K
Density of ambient ISM	n_a	0.1 cm^{-3}
Radius of jet-blown bubble	$R_{\mathrm{[Fe\ II]}}$	175 pc
Eastern jet flux†	$F_{E,\mathrm{East\ lobe}}$	1.50×10^{44} erg s^{-1}
Western jet flux†	$F_{E,\mathrm{West\ lobe}}$	1.44×10^{44} erg s^{-1}
Total jet flux	F_E	2.94×10^{44} ergs^{-1}

Assuming that half of the energy injected by the jets goes into pdV work on the surrounding ISM and the other half into the energy density in both particles and magnetic field, then the total energy in the lobes after a time t_{lobe} is given by

$$F_{\mathrm{lobe}} = \frac{1}{t_{\mathrm{lobe}}}\frac{1}{2}\sum_{\mathrm{min},i}\varepsilon_i V_i \tag{5}$$

where V_i is the volume and ε_i is the minimum energy computed using Eq. 3. Assuming an upper limit for the age of the lobes $t_{\mathrm{lobe}} = 5000$ yr from Gi03 based on synchrotron spectral decay, we find $F_{E,\mathrm{West\ lobe}} = 1.5\times10^{44}$ erg s^{-1} and $F_{E,\mathrm{Eastern\ lobe}} = 1.1\times10^{44}$ erg s^{-1}.

5.2 The origin of the [Fe II] emission

Fast shocks destroy dust grains, releasing Fe I into the gas phase, which then becomes singly ionised by the interstellar radiation field.

In the post-shock region, Fe II becomes collisionally excited and emits emission lines in the near-IR, including [Fe II], which can therefore be used as a shock tracer.

Fig. 2 shows that the [Fe II] emission is localised to the innermost few 100 pc of the nucleus, and that the radial velocity field is consistent with material being launched out of the disc plane on either side. The kinematics and location of the [Fe II] emission suggest that it arises from shocks driven by the expanding bubble inflated by the radio jets.

However, SNe explosions can also give rise to strong [Fe II] emission; we now determine whether this is plausible. To calculate the required SNe rate to produce the observed [Fe II] emission, we use the empirical relationship between SN rate and [Fe II]$_{\lambda 1.26}$ luminosity for starburst galaxies derived by Rosenberg et al. (2012):

$$\log \frac{\nu_{\mathrm{SNrate}}}{\mathrm{yr}^{-1}} = (1.01 \pm 0.2) \log \frac{L_{[\mathrm{Fe\ II}]_{\lambda 1.26}}}{\mathrm{erg\ s}^{-1}} - (41.17 \pm 0.9) \quad (6)$$

Because [Fe II]$_{\lambda 1.26}$ lies outside the wavelength range of our observations, we assume any reddening is negligible and use the intrinsic ratio [Fe II] 1.26/1.64 μm = 1.36. The integrated luminosity is given by $L([\mathrm{Fe\ II}]_{\lambda 1.644}) = 4\pi D_L^2 F_{[\mathrm{Fe\ II}]_{1.644}} = 5.6 \times 10^{38}$ erg s^{-1} where $F_{[\mathrm{Fe\ II}]_{\lambda 1.644}}$ is the integrated flux (Table 1) and the luminosity distance D_L = 271.3 Mpc. Using Eq. 6 yields an integrated SN rate $\nu_{\mathrm{SN\ rate,\ [Fe\ II]}} = 0.0126$ yr^{-1}.

We now use the measured SFR of to estimate ν_{SNrate} using a solar metallicity Starburst99 (Leitherer et al. 1999) model with a continuous 1 M$_\odot$ yr^{-1} SF law and a Salpeter IMF at an age of 1 Gyr. After multiplying to match the SFR of 4C 31.04 (4.9 $M_\odot$ yr^{-1} (Ocaña Flaquer et al. 2010)) we find $\nu_{\mathrm{SNrate,\ SFR}} = 0.1$ yr^{-1}, higher than the rate required to power the [Fe II] emission.

Therefore we cannot unequivocally rule out star formation as the excitation mechanism for the [Fe II]. We nonetheless argue that the emission is driven by a jet-ISM interaction, as the kinematics are consistent with an expanding bubble localised to the inner few 100 pc of the nucleus. Therefore we propose that the [Fe II] traces gas that has been processed by the forward shock of the jet-driven bubble. As illustrated in Fig. 10, the bubble drives fast shocks into the ISM, destroying molecular gas. The shocked gas is accelerated outwards by the forward shock and also by the jet streams, creating an expanding bubble illuminated in [Fe II].

5.3 The origin of the H_2 emission

Large masses of warm H_2 seem to be common in the hosts of nearby radio galaxies, suggesting a link between the H_2 emission and radio activity (e.g., Nesvadba et al. 2010; Ogle et al. 2010). As discussed in Section 4.2, we detect ro-vibrational H_2 emission in the circumnuclear disc ≈ 2 kpc in diameter, which probes relatively hot ($\sim 10^3$ K) molecular gas. The line ratios show the warm H_2 is shock excited (Table 2 and Fig. 7).

In this section, we show that the $\sim 10^3$ K H_2 represents a relatively hot fraction of a much larger reservoir of H_2 heated by a jet-ISM interaction, the bulk of which is much cooler ($\sim 10^2$ K). As shown in Fig. 10, the jet-driven bubble drives fast shocks into the gas at small radii, causing [Fe II] emission, before decelerating as it drives shocks into the more dense molecular gas in the disc. Jet plasma percolating radially throughout the disc accelerates clouds to the observed systemic blueshift of $\approx$ 150km s^{-1} in the warmer H_2 component (Fig. 3).

5.3.1 *Excitation mechanism*

The ro-vibrational-emitting H_2 probed by our observations is very warm (Fig. 6), and cools rapidly. This phase is therefore very short-lived, and accordingly only represents a very small fraction of the total H_2 mass (Table 3). Willett et al. (2010) report a much larger ($\sim 10^6 M_\odot$) reservoir of cooler H_2, at a temperature $\sim 300K$. We wish to determine whether this component represents gas in the circumnuclear disc that has been processed by the jets and since cooled; to do this we use mid-IR diagnostics to reveal the excitation mechanism of the cooler H_2 component.

Using the combined luminosity of the H_2 0–0 S(0,1,2,3) lines (Willett et al. 2010) we place a lower limit on the ratio $L(H_2)/L(\mathrm{PAH\ 7.7\ }\mu\mathrm{m}) \geq 0.1$, where we calculate the luminosity of the PAH feature at 7.7 μm using that of the 11.3 μm and assuming $L(\mathrm{PAH\ 6.2\ }\mu\mathrm{m})/L(\mathrm{PAH\ 7.7\ }\mu\mathrm{m}) = 0.26$, which holds for the sample of H_2-luminous radio galaxies of Ogle et al. (2010); this gives $L(\mathrm{PAH\ 7.7}) = 1.55 \times 10^{42}$ erg s^{-1}. The criterion of Ogle et al. (2010) (> 0.04) strongly suggests the H_2 is shock heated.

We also use the diagnostic diagram (Fig. 6) of Nesvadba et al. (2010), which separates star formation from other mechanisms as the source of H_2 heating using the luminosity ratios of the summed H_2 0–0 S(0)–S(3) lines to the ^{12}CO(1 – 0) and to the PAH feature at 7.7 μm. Whilst the CO emission traces cold molecular gas from which stars form, PAH features trace UV photons excited by star formation; hence these ratios can be used to indicate the contribution of star formation in photon-dominated regions (PDRs) to the H_2 heating. To calculate the CO(1-0) luminosity, we convert the I_{CO} given by Ocaña Flaquer et al. (2010) into a luminosity using Eqn. 3 of Solomon et al. (1997), yielding $L(\mathrm{CO}) = 3.56 \times 10^{38}$ erg s^{-1}. We find $L_{H_2}/L(\mathrm{PAH\ 7.7}) \geq 0.148$ and $L_{H_2}/L(\mathrm{CO}) \geq 6.43 \times 10^2$, placing 4C 31.04 well outside the regions covered by PDR models, showing that the ~ 300 K H_2 component is not predominantly heated by UV photons, leaving shocks, cosmic rays and X-ray heating as plausible mechanisms.

Based on our above arguments, both the ~ 100 K and $\sim 10^3$ K H_2 is heated by a mechanism other than star formation. We argue that the $\sim 10^3$ K and $\sim 100K$ H_2 are physically associated; in this case the strong shock signature we observe in the former (Fig. 7) shows that the warm H_2 is shock excited.

5.3.2 *What is driving the shocks?*

We now show that the observed H_2 luminosity cannot be produced by shocks driven by gas accreting onto the disc. The energy dissipated by gas accreting onto the disc at a rate $\dot{M}$ from $r = \infty$ to $r = r_0$ is given by

$$L_{\mathrm{disc}} = \frac{1}{2}\dot{M} v_c(r)^2 + \Phi(r)\dot{M} \quad (7)$$

where $\Phi(r)$ is the galactic potential and $v_c(r)$ is the velocity of a circular orbit at radius r. We assume that the jet-driven bubble disrupts accretion at smaller radii, hence we use r_0 = 175 pc, the approximate extent of the [Fe II] emission.

To obtain $\Phi(r)$ and $v_c(r)$, we fit a simple $1/n$ Sersić profile to the K-band continuum and use the analytical expressions given by Terzić & Graham (2005). We estimate the stellar mass from the 2MASS K_s-band magnitude using a simple stellar population model of Bruzual & Charlot (2003) with a single instantaneous burst of star formation, assuming solar metallicity, a Chabrier IMF and an age of a few Gyr. This yields $\log M_* \approx 11.4$.

If $\dot{M}$ is also equal to the accretion rate of the black hole, and that the 10% of the rest-mass energy of the accreted material

per unit time is emitted in the form of the radio jets, i.e., $L_{\rm BH} = 0.1\dot{M}c^2 = 2.944 \times 10^{44}$ erg s^{-1}, then the accretion rate $\dot{M} \approx 0.05 M_\odot$ yr^{-1}, and using Eqn. 7, an accretion disc luminosity $L_{\rm disc} \sim 10^{40}$ erg s^{-1}, an order of magnitude lower than the observed H_2 0–0 luminosity $L_{H_2} \geq 2.3 \times 10^{41}$ erg s^{-1}, enabling us to rule out accretion as the mechanism heating the H_2. Meanwhile, the H_2 luminosity represents $\sim 0.1\%$ of the estimated jet flux (Section 5.1). We therefore conclude that the shocks are being driven by the jets, a scenario which also explains the sharp peak in the H_2 flux in the vicinity of the nucleus (Fig. 3).

Shocks induced by a jet-ISM interaction out to kpc-scale radii in the circumnuclear disc could explain the peculiar systemic blueshift of ≈ 150 km s^{-1} we observe in the H_2 (Fig. 3) relative to the redshift $z = 0.0602$ of Ga07. Previous observations have revealed additional cold gas components with a remarkably similar blueshifts: Ga07 detected an unresolved HCO^+ component in absorption over the nucleus with a systemic blueshift of ≈ 150 km s^{-1}. Struve & Conway (2012) found that the centre of the integrated H I absorption profile is centered on a similar blueshifted systemic velocity. The absorption profile also has a blue wing (their Fig. 7) extending to ~ 200 km s^{-1}. Prominent blue wings in the H I absorption profiles of powerful radio galaxies are a signature of fast neutral outflows (Morganti et al. 2005); we speculate that the blue wing in the profile of 4C 31.04 indicates that the jets are accelerating H I out of the galaxy, albeit to much lower velocities.

It is possible that the systemic velocity we measure for the H_2 represents that of the host galaxy, and that the redshift is in fact lower than currently thought. Ga07 determined this value by assuming that the HCO^+ emission components to the North and South of the nucleus represented gas rotating in the disc, and that the mean velocity of the two components corresponds to the galaxy's systemic velocity. Struve & Conway (2012) argue that this assumption may be flawed if gas in the disc is dynamically unsettled. Correcting the redshift to match the systemic velocity of the $\sim 10^3$ K H_2, H I and HCO^+ absorption yields $z = 0.0597 \pm 0.001$. Whilst this is consistent with the redshift from optical spectroscopy ($z = 0.060 \pm 0.001$, Marcha et al. (1996)), it would mean the [Fe II] emission is in fact redshifted by ≈ 150 km s^{-1}, which would be difficult to explain under our interpretation that it traces a jet-driven bubble.

Rather, the blueshifted warm and cold molecular phases may trace clouds of gas being radially accelerated in circumnuclear disc by jet plasma. As mentioned earlier, hydrodynamical simulations by Mukherjee et al. (2018a) of jets evolving in galaxies with clumpy gas discs have shown that the expanding bubble driven by the jet drives subrelativistic radial flows into the disc plane. These flows drive turbulence and shocks into the gas, and introduce significant non-circular motions. In addition to the observed blueshifted gas, radial flows of jet plasma may be able to explain the reported unrelaxed dynamics in the gas disc (Pe01; Ga07), which has previously been attributed to gas settling onto the disc in the process of accretion. We note that ~ 100 pc-scale equatorial outflows have been recorded in other radio galaxies, such as NGC 5929 (Riffel et al. 2015) and NGC 1386 (Lena et al. 2015). These outflows have tentatively been attributed to torus outflows or accretion disc winds; it is unclear whether this mechanism could drive the relatively low-velocity blueshifted gas we observe in 4C 31.04.

We now calculate the kinetic energy associated with the observed blueshift in the H_2 to show that it is plausible that it is driven by the jets. Assuming that both the ~ 100 K and $\sim 10^3$ K H_2 are accelerated to the observed blueshifted velocity, the cooler component ($4.7 \pm 1.3 \times 10^6$ $M_\odot$ (Willett et al. 2010)) will dominate the kinetic energy. If the blueshifted clouds have a velocity 150 km s^{-1}, then the associated kinetic energy is $\approx 1.1 \times 10^{54}$ erg. Assuming the gas is being pushed radially outwards at a constant velocity, the time taken for material to reach the farthest extent of the warm H_2 disc ≈ 1 kpc from the nucleus is $\tau = 6.5 \times 10^6$ yr. Assuming the jet has been accelerating this gas over this time period, this yields an energy injection rate $\sim 10^{41}$ erg s^{-1}, approximately 0.1% of the jet power we estimated in Section 5.1, showing that it is indeed plausible.

In light of these arguments, we tentatively agree with the redshift quoted by Ga07, and speculate that the blueshifted H_2, H I and HCO^+ traces gas clouds being radially accelerated in the disc plane by the jet plasma. Confirmation of this scenario will require further observations, e.g., high-resolution optical spectroscopy to measure the galaxy's redshift using stellar absorption features.

5.3.3 *How far does the jet plasma extend?*

In the previous sections we have shown that both the [Fe II] and H_2 emission are caused by a jet-ISM interaction. However, the radio lobes extend ≈ 60 pc from the nucleus, whereas we detect [Fe II] over a region ≈ 3 times larger, and warm H_2 out to $\sim$ kpc radii—how could this emission possibly arise from a jet-ISM interaction?

Hydrodynamical simulations of jets propagating into clumpy discs (Mukherjee et al. 2018a) show that the brightest regions of jet plasma may become temporarily frustrated by dense clouds in the disc, slowing its propagation. This effect becomes more pronounced when the jets are inclined with respect to the disc normal, as it increases the effective path length over which the jets interact with the dense ISM. Meanwhile, the expanding bubble can advance rapidly once it escapes the dense ISM in the disc plane, allowing the bubble radius to grow several times larger than the radio lobes.

Our observations show the jets in 4C 31.04 are likely to be inclined $\sim 10^\circ - 20^\circ$ to the normal of the circumnuclear disc. This geometry is supported by the inclination of $\sim 60^\circ$ we measure from the warm H_2 and by the jets being at an angle of $\lesssim 15^\circ$ with respect to the sky, with the Western lobe nearest (Giovannini et al. 2001). Moreover, the kinematics of the [Fe II] emission line (2) shows material being accelerated off the disc plane such that the Western lobe is pointing towards us.

In order to illustrate the role that a dense and clumpy disc can play in determining the outcome of a jet-ISM interaction, we show midplane density and temperature slices from a hydrodynamical simulation[5] in which the jets are inclined 20° to the disc normal in Fig. 8. In 8 (a), the brightest parts of the jet plasma (magenta contours), particularly in the +ve Z-direction, have become halted a short distance from the nucleus. Meanwhile, lower surface brightness plasma (black contours) propagates along channels in the clumpy ISM and fills the much larger bubble, which crucially may go undetected in high-resolution VLBI observations despite interacting strongly with the surrounding ISM. In Fig. 9 we show corresponding synthetic 1 GHz surface brightness maps with high (a) and low (b) dynamic ranges[6]. Comparing the two illustrates the importance of a high dynamic range in revealing the low surface brightness plasma that traces the true extent of the jet-driven bubble.

Multiple flux completeness measurements of VLBI observations of 4C 31.04 indeed suggest that some large-scale structure could exist at lower surface brightnesses than have been observed.

[5] Simulation C of Mukherjee et al. (2018a); for details see their Table 2.
[6] We define dynamic range as the maximum measured flux divided by the minimum flux level that can be detected.

Cotton et al. (1995) find that 98% and 76% of the flux density of 4C 31.04 measured with the VLA is recovered in VLBI observations at 1.7 and 8.4 GHz respectively. Gi03 find that approximately 90% of the flux measured with single-dish observations is recovered with VLBI at 5 GHz. Altschuler et al. (1995) recover 80% of the total flux density at 92 cm. We note that the 5 GHz VLBI image of Gi03 has a dynamic range of $\sim$ 100; this, combined with the $\sim$ 75 – 95% flux completeness of GHz-range VLBI observations, suggests that 4C 31.04 may indeed harbour low surface brightness radio emission out to the radii at which we observe shocked gas, resolving the inconsistency between the extent of the shocked gas and the radio lobes.

5.4 Age of the radio source

We cannot estimate the true age of the radio jets in 4C 31.04 with existing VLBI observations as they resolve out low surface brightness radio emission that fills a much larger bubble revealed by our NIFS observations. We instead use the jet flux and our NIFS observations to estimate the true age of the radio jets.

We model the radio lobes as bubbles expanding adiabatically into a uniform ISM using the model of Bicknell & Begelman (1996). We assume that the bubbles are expanding out of the disc plane into the ambient hot ISM with $p/k \sim 10^6$ K cm^{-3} typical in the interiors of local elliptical galaxies (Werner et al. 2012) and $T_a \sim 10^7$ K, $n_a = p/kT_a \approx 0.1$ cm^{-3}. The age of the bubble is given by

$$t_b = \left(\frac{384\pi}{125}\right)^{1/3} \rho_a^{1/3} F_E^{-1/3} R_b^{5/3} \tag{8}$$

where R_b is the radius of the bubble and F_E is the total jet flux in erg s^{-1}.

We calculate a lower limit for the age of the radio source by assuming that the jet plasma has only reached the extent of the [Fe II] emission, ignoring the extended H_2 emission. In this case, we set $R_b \approx 175$ pc and find $t_b \approx 17$ kyr, more than 3 times older than the age estimated using synchrotron spectral decay (4000-5000 yr, Giroletti et al. (2003)).

In Section 5.3.2, we estimated an upper limit for the jet age by calculating the time taken for material to reach the farthest extent of the warm H_2 disc, $\approx 6.5 \times 10^6$ yr, and is an upper limit as the gas may have decelerated along its trajectory.

Although these age estimates are very crude, together they show that the previous age estimates based on VLBI imaging alone do not represent the true age of the source. Our results demonstrate the importance of optical or near-IR tracers of jet-ISM interaction in estimating the true extent of the jet plasma, particularly when existing radio observations have a low dynamic range or are not sensitive to the angular scales associated with the diffuse plasma filling the jet-driven bubbles.

5.5 Density distribution of the clumpy ISM

Free-free absorption (FFA) by clumpy gas ionised by the radio jets is the most likely cause of the spectral turnover in GPS and CSS sources (Bicknell et al. 2018). Here, we use the peak in the radio spectrum of 4C 31.04 to infer the parameters of the density distribution of the ionised, free-free absorbing ISM, in order to inform future hydrodynamical simulations.

We use a simple analytical model to calculate the specific intensity of synchrotron-emitting plasma embedded in a clumpy free-free absorbing medium. We assume the density n of the ionised medium follows a log normal distribution, which is appropriate for a turbulent medium (e.g., Federrath & Klessen 2012)[7]. We assume that the only ions contributing to FFA are H^+, He^+ and He^{++}, and that the absorption coefficients α_ν are constant along the line of sight. For a species i with charge Z the linear absorption coefficient is

$$\alpha_{\nu,i}(Z) = n^2 \cdot \sqrt{\frac{32\pi}{27}} c^2 r_0^3 \left(\frac{kT}{m_e c^2}\right)^{-3/2} \frac{n_e}{n} \frac{n_i(Z)}{n} Z^2 g_\nu(T,Z) \nu^{-2} \tag{10}$$

where $n_i(Z)$ and n_e are the species and electron number densities respectively, T is temperature, Z is the charge and $g(T,Z)$ is the Gaunt factor, and we divide by n^2 so that the ion abundances can be expressed as fractions. The FFA optical depth is given by

$$\begin{aligned}\tau_\nu &= (\alpha_{\nu,\,H^+} + \alpha_{\nu,\,He^+} + \alpha_{\nu,\,He^{++}})L \\ &= E(n^2)\left(\frac{\alpha_{\nu,\,H^+} + \alpha_{\nu,\,He^+} + \alpha_{\nu,\,He^{++}}}{E(n^2)}\right)L\end{aligned} \tag{11}$$

where L is the depth of the absorbing screen and we have substituted the expected value $E(n^2) = e^{2(m+s^2)}$ for n^2 in Eqn. 10. We assume that the 100 pc-scale jets ionise clouds of material on the inner edge of the circumnuclear disc, which then free-free absorb radio emission from the jet plasma. This is consistent with the high-velocity H I clouds and regions of free-free absorbed 1.4 GHz continuum emission detected in front of both lobes (Conway 1996). Hence we take $L = 100$ pc.

The width s of the log-normal distribution can be related to the properties of the ISM using

$$s^2 = \ln\left(1 + b^2\mathcal{M}^2\frac{\beta}{\beta+1}\right) \tag{12}$$

which applies when the magnetic field strength $B \propto \rho^{1/2}$ (Federrath & Klessen 2012). Here, b is the turbulent forcing parameter, β is the ratio of thermal to magnetic pressure and $\mathcal{M} = \sigma_v/c_s$ is the Mach number where σ_v is the velocity dispersion and $c_s = \sqrt{kT/\mu' \text{amu}}$ is the sound speed. We assume the velocity dispersion of the absorbing medium is equivalent to the stellar velocity dispersion, which we estimate from the 2MASS K-band Faber-Jackson relation of Meylan et al. (2006). From s^2 we can calculate m and and therefore the mean density $E(n) = \mu$ and width σ of the distribution using

$$\begin{aligned}\mu &= e^{m+\frac{1}{2}s^2} \\ \sigma^2 &= \mu^2\left(e^{s^2} - 1\right).\end{aligned} \tag{13}$$

Table 5 lists the values of our input parameters. We use a MAPPINGS V (Sutherland et al. 2013) model grid with non-equilibrium cooling and solar abundances to compute the fractional abundances of electrons, H^+, He^+ and He^{++}. Assuming $\tau_\nu \sim 1$ at the spectral peak, we find the mean density of the ionised medium $\mu = 17.0$cm^{-3} and the standard deviation in the density $\sigma = 136$ cm^{-3}.

[7] The log normal distribution has the probability distribution function

$$P(n) = \frac{1}{\sqrt{2\pi}s}\exp\left[-\frac{(\ln n - m)^2}{2s^2}\right] \tag{9}$$

which is a Gaussian in $\ln n$, where m is the mean log density and s is the width of the distribution in log density. (e.g., SB07).

Table 5. Parameters used in determining the parameters of the log-normal density distribution. Output parameters are denoted with daggers (†).

Parameter	Symbol	Value
Peak frequency	$\nu_{\rm peak}$	400 MHz
Depth of absorbing slab	L	100 pc
Temperature	T	10059 K
Mean molecular mass	μ'	0.66504
Electron fractional abundance	n_e/n	0.47175
H^+ fractional abundance	n_{H^+}/n	0.41932
He^+ fractional abundance	n_{He^+}/n	0.024458
He^{++} fractional abundance	$n_{He^{++}}/n$	0.013770
Velocity dispersion	σ_v	318 km s^{-1}
Turbulent forcing parameter	b	0.4
Ratio of thermal to magnetic pressure	β	1 (equipartition)
Expected value of $n^{2\dagger}$	$E(n^2)$	1.89×10^4 cm^{-6}
Mean density†	μ	17.0 cm^{-3}
Density variance†	σ^2	1.86×10^4 cm^{-6}

6 CONCLUSION

We report *H*- and *K*-band NIFS observations of the Compact Steep Spectrum source 4C 31.04, a young AGN with jets interacting strongly with a clumpy ISM. The host of 4C 31.04 is a $z = 0.0602$ elliptical galaxy that harbours $\sim 10^9$ M$_\odot$ of gas located in circumnuclear disc ≈ 2 kpc in diameter.

In the central few 100s pc, we detect [Fe II] emission that has a radial velocity field consistent with an expanding bubble driven by the jets. Although we cannot rule out SNe explosions as the cause of the [Fe II] emission, the kinematics of the line trace an expanding bubble, implying the emission is a result of a jet-ISM interaction.

We also detect ro-vibrational H_2 emission that traces $\sim 10^3$ $M_\odot$ of warm ($\sim 10^3$ K) H_2. This warm molecular phase traces rapidly cooling gas in the innermost $\sim$ kpc of the circumnuclear disc, and represents a small fraction of a much larger ($\sim 10^6$ $M_\odot$) reservoir of cooler ($\sim 10^2$ K) H_2. Near- and mid-IR line ratios indicate both H_2 components are excited by shocks. We show that accretion of gas onto the kpc-scale circumnuclear disc is unable to reproduce the observed H_2 luminosity, and conclude that the shocks must be driven by jet plasma percolating to kpc radii through channels in the clumpy disc. The $\sim 10^3$ K H_2 emission shows a systemic blueshift of $\approx$ 150 km s^{-1} relative to the most widely accepted redshift of Ga07. We speculate that the blueshift is caused by jet plasma radially accelerating clouds in the disc plane to kpc radii. Previous observations of 4C 31.04 have revealed spatially-unresolved HCO^+ and H I in absorption at similarly blueshifted velocities, which may represent cooler gas entrained in the same low-speed outflow. The blueshift could also be explained if the redshift of the galaxy is in fact lower than currently believed, although this would impart a significant redshift to our [Fe II] observations which would be difficult to explain.

Our observations demonstrate that 4C 31.04 is currently in the 'flood-and-channel' phase of evolution that has been predicted by hydrodynamical simulations (e.g., Mukherjee et al. 2016; Sutherland & Bicknell 2007), in which streams of jet plasma follow paths of least resistance through the ISM and form an energy-driven bubble. The bubble pushes a forward shock into the ambient ISM, giving rise to the [Fe II] emission. Jet plasma also percolates into the circumnuclear disc, shocking and radially accelerating gas clouds, giving rise to the H_2 emission.

The extent of the shocked gas in our NIFS observations is much larger than the radio lobes resolved in VLBI imaging, suggesting the presence of low surface brightness radio plasma that has not been previously observed. This is consistent with multi-frequency VLBI observations of 4C 31.04 with < 100% flux completeness. In simulations of jets propagating through clumpy discs, the brightest regions of plasma can become temporarily halted by dense clumps, whilst the lower density plasma channels can continue to expand freely out of disc plane, enabling the bubble to grow much larger than the jets resolved by low-dynamic range VLBI observations.

We estimated the jet flux using VLBI observations and use the observed bubble radius to constrain the 'true' age of the radio jets. We find the jet age $\gtrsim$ 17.6 kyr, much older than previous literature estimates derived from the lobe expansion rate and using synchrotron spectral decay (Giroletti et al. 2003).

Finally, we calculated the parameters of the density distribution of the ISM from the peak of the radio spectrum using a FFA model. These parameters together with our estimates of the jet flux will be used to inform future hydrodynamical systems tailored to 4C 31.04.

Our observations of 4C 31.04 demonstrate that optical and near-IR studies of radio galaxies can be crucial in estimating determining the true extent of the radio plasma, particularly in the early stages of evolution in which low surface brightness radio plasma may be resolved out by VLBI observations.

ACKNOWLEDGEMENTS

This study is based on observations obtained at the Gemini Observatory (processed using the Gemini IRAF package), which is operated by the Association of Universities for Research in Astronomy, Inc., under a cooperative agreement with the NSF on behalf of the Gemini partnership: the National Science Foundation (United States), the National Research Council (Canada), CONICYT (Chile), Ministerio de Ciencia, Tecnología e Innovación Productiva (Argentina), and Ministério da Ciência, Tecnologia e Inovação (Brazil). The authors thank Alice Quillen for helpful discussions. The authors also wish to recognize and acknowledge the very significant cultural role and reverence that the summit of Mauna Kea has always had within the indigenous Hawai'ian community.

REFERENCES

Altschuler D. R., Gurvits L. I., Alef W., Dennison B., Graham D., Trotter A. S., Carson J. E., 1995, A&AS, 114, 197
Bicknell G. V., 2002, New Astron. Rev., 46, 365
Bicknell G. V., Begelman M. C., 1996, ApJ, 467, 597
Bicknell G. V., Sutherland R. S., van Breugel W. J. M., Dopita M. A., Dey A., Miley G. K., 2000, ApJ, 540, 678
Bicknell G. V., Mukherjee D., Wagner A. Y., Sutherland R. S., Nesvadba N. P. H., 2018, MNRAS, 475, 3493
Bruzual G., Charlot S., 2003, MNRAS, 344, 1000
Callingham J. R., et al., 2017, ApJ, 836, 174
Conway J. E., 1996, in Ekers R. D., Fanti C., Padrielli L., eds, IAU Symposium Vol. 175, Extragalactic Radio Sources. p. 92
Cotton W. D., Feretti L., Giovannini G., Venturi T., Lara L., Marcaide J., Wehrle A. E., 1995, ApJ, 452, 605
Croton D. J., et al., 2006, MNRAS, 365, 11
Dale D. A., Sheth K., Helou G., Regan M. W., Hüttemeister S., 2005, AJ, 129, 2197
Federrath C., Klessen R. S., 2012, ApJ, 761, 156
Fragile P. C., Anninos P., Croft S., Lacy M., Witry J. W. L., 2017, ApJ, 850, 171
Gaibler V., Khochfar S., Krause M., Silk J., 2012, MNRAS, 425, 438

García-Burillo S., Combes F., Neri R., Fuente A., Usero A., Leon S., Lim J., 2007, A&A, 468, L71
Giovannini G., Cotton W. D., Feretti L., Lara L., Venturi T., 2001, ApJ, 552, 508
Giroletti M., Giovannini G., Taylor G. B., Conway J. E., Lara L., Venturi T., 2003, A&A, 399, 889
Gonçalves A. C., Serote Roos M., 2004, A&A, 413, 97
King A., Pounds K., 2015, ARA&A, 53, 115
Lacy M., Croft S., Fragile C., Wood S., Nyland K., 2017, ApJ, 838, 146
Leitherer C., et al., 1999, ApJS, 123, 3
Lena D., et al., 2015, ApJ, 806, 84
Maccagni F. M., Santoro F., Morganti R., Oosterloo T. A., Oonk J. B. R., Emonts B. H. C., 2016, A&A, 588, A46
Marcha M. J. M., Browne I. W. A., Impey C. D., Smith P. S., 1996, MNRAS, 281, 425
Markwardt C. B., 2009, in Bohlender D. A., Durand D., Dowler P., eds, Astronomical Society of the Pacific Conference Series Vol. 411, Astronomical Data Analysis Software and Systems XVIII. p. 251 (arXiv:0902.2850)
McGregor P. J., et al., 2003, in Iye M., Moorwood A. F. M., eds, Proc. SPIEVol. 4841, Instrument Design and Performance for Optical/Infrared Ground-based Telescopes. pp 1581–1591, doi:10.1117/12.459448
Meylan G., Jetzer P., North P., Schneider P., Kochanek C. S., Wambsganss J., eds, 2006, Gravitational Lensing: Strong, Weak and Micro (arXiv:astro-ph/0407232)
Moré J. J., 1978, The Levenberg-Marquardt algorithm: Implementation and theory. Springer Berlin Heidelberg, Berlin, Heidelberg, pp 105–116, doi:10.1007/BFb0067700, https://doi.org/10.1007/BFb0067700
Morganti R., Tadhunter C. N., Oosterloo T. A., 2005, A&A, 444, L9
Morganti R., Fogasy J., Paragi Z., Oosterloo T., Orienti M., 2013, Science, 341, 1082
Morganti R., Oosterloo T., Oonk J. B. R., Frieswijk W., Tadhunter C., 2015, A&A, 580, A1
Mukherjee D., Bicknell G. V., Sutherland R., Wagner A., 2016, MNRAS, 461, 967
Mukherjee D., Bicknell G. V., Wagner A. Y., Sutherland R. S., Silk J., 2018a, preprint, (arXiv:1803.08305)
Mukherjee D., Wagner A. Y., Bicknell G. V., Morganti R., Oosterloo T., Nesvadba N., Sutherland R. S., 2018b, MNRAS, 476, 80
Nesvadba N. P. H., et al., 2010, A&A, 521, A65
Nesvadba N. P. H., Boulanger F., Lehnert M. D., Guillard P., Salome P., 2011, A&A, 536, L5
O'Dea C. P., 1998, PASP, 110, 493
Ocaña Flaquer B., Leon S., Combes F., Lim J., 2010, A&A, 518, A9
Ogle P., Boulanger F., Guillard P., Evans D. A., Antonucci R., Appleton P. N., Nesvadba N., Leipski C., 2010, ApJ, 724, 1193
Perlman E. S., Stocke J. T., Conway J., Reynolds C., 2001, AJ, 122, 536
Puxley P. J., Hawarden T. G., Mountain C. M., 1990, ApJ, 364, 77
Riffel R. A., Vale T. B., Storchi-Bergmann T., McGregor P. J., 2014, MNRAS, 442, 656
Riffel R. A., Storchi-Bergmann T., Riffel R., 2015, MNRAS, 451, 3587
Rosenberg M. J. F., van der Werf P. P., Israel F. P., 2012, A&A, 540, A116
Rosenberg M. J. F., van der Werf P. P., Israel F. P., 2013, A&A, 550, A12
Salomé Q., Salomé P., Combes F., 2015, A&A, 574, A34
Salomé Q., Salomé P., Miville-Deschênes M.-A., Combes F., Hamer S., 2017, A&A, 608, A98
Scharwächter J., McGregor P. J., Dopita M. A., Beck T. L., 2013, MNRAS, 429, 2315
Serote Roos M., Gonçalves A. C., 2004, A&A, 413, 91
Silk J., Rees M. J., 1998, A&A, 331, L1
Solomon P. M., Downes D., Radford S. J. E., Barrett J. W., 1997, ApJ, 478, 144
Storchi-Bergmann T., Riffel R. A., Riffel R., Diniz M. R., Borges Vale T., McGregor P. J., 2012, ApJ, 755, 87
Struve C., Conway J. E., 2012, A&A, 546, A22
Sutherland R. S., Bicknell G. V., 2007, ApJS, 173, 37
Sutherland R., Dopita M., Binette L., Groves B., 2013, MAPPINGS III: Modelling And Prediction in PhotoIonized Nebulae and Gasdynamical Shocks, Astrophysics Source Code Library (ascl:1306.008)
Tadhunter C., Morganti R., Rose M., Oonk J. B. R., Oosterloo T., 2014, Nature, 511, 440
Terzić B., Graham A. W., 2005, MNRAS, 362, 197
Tingay S. J., et al., 2015, AJ, 149, 74
Tremaine S., et al., 2002, ApJ, 574, 740
Wagner A. Y., Bicknell G. V., 2011, ApJ, 728, 29
Wagner A. Y., Bicknell G. V., Umemura M., Sutherland R. S., Silk J., 2016, Astronomische Nachrichten, 337, 167
Werner N., Allen S. W., Simionescu A., 2012, MNRAS, 425, 2731
Willett K. W., Stocke J. T., Darling J., Perlman E. S., 2010, ApJ, 713, 1393
Wolniewicz L., Simbotin I., Dalgarno A., 1998, ApJS, 115, 293
Wright E. L., 2006, PASP, 118, 1711
Zubovas K., Bourne M. A., 2017, MNRAS, 468, 4956
van Breugel W., Miley G., Heckman T., 1984, AJ, 89, 5

This paper has been typeset from a TEX/LATEX file prepared by the author.